

A self-consistent stellar and 3D nebular model for Planetary Nebula IC418

C. Morisset and L. Georgiev

Instituto de Astronomía, Universidad Nacional Autónoma de México
Apdo. postal 70–264; Ciudad Universitaria; México D.F. 04510; México.
e-mail: Chris.Morisset@gmail.com and Georgiev@astroscu.UNAM.mx

Received May, 2009; accepted September, 2009

ABSTRACT

Aims. We present a coherent stellar and nebular model reproducing the observations of the Planetary Nebula IC418. We want to test whether a stellar model obtained by fitting the stellar observations is able to satisfactorily ionize the nebula and reproduce the nebular observations, which is by no means evident. This allows us to determine all the physical parameters of both the star and the nebula, including the abundances and the distance.

Methods. We used all the observational material available (FUSE, IUE, STIS and optical spectra) to constrain the stellar atmosphere model performed using the CMFGEN code. The photoionization model is done with Cloudy_3D, and is based on CTIO, Lick, SPM, IUE and ISO spectra as well as HST images. The aperture sizes and positions of the different observations are taken into account. More than 140 nebular emission lines are compared to the observed intensities. The distance is determined using evolutionary tracks.

Results. We reproduce all the observations for the star and the nebula. The 3D morphology of the gas distribution is determined. The effective temperature of the star is 36.7 ± 0.5 kK. Its luminosity is $7700 L_{\odot}$. We describe an original method to determine the distance of the nebula using evolutionary tracks. No clumping factor is needed to reproduce the age-luminosity relation. The distance of 1.25 kpc is found in very good agreement with recent determination using parallax method, and the age of the nebula is estimated to be 1400 years. The chemical composition of both the star and the nebula are determined. Both are Carbon-rich. The nebula presents evidence of depletion of elements Mg, Si, S, Cl (0.5 dex lower than solar) and Fe (2.9 dex lower than solar), indicating a depletion of these elements into grains.

Conclusions. This is the first self-consistent stellar and nebular model for a Planetary Nebula that reproduces all the available observations ranging from IR to UV, showing that the combined approach for the modeling process leads to more restrictive constraints and, in principle, more trustworthy results.

Key words. methods: numerical – planetary nebulae – individual object: IC418

1. Introduction

Planetary Nebulae (PNe) are the ultimate visible stage of the evolution of intermediate mass stars. They consist in an extended shell photoionized by a central hot remnant (a white dwarf). The determination of the chemical composition of PNe is important for various reasons. It allows to put important observational constraints on the models of nucleosynthesis in intermediate mass stars (e.g. Marigo et al. 2003). It also allows one to trace the metallicity of the medium out of which the progenitor star was born, if using elements (S, Ar) whose abundances are not expected to be modified in the external layers of the PN progenitor during its evolution. Finally, it gives some clues on the depletion of metals onto dust grains produced by the PN progenitor.

Abundance determinations in planetary nebulae are obtained either by empirical methods, directly from the observed spectra, or through photoionization modeling. In principle, a photoionization model is expected to give more reliable abundances, since these are obtained in a way that accounts for the temperature and ionization structure of the nebula. However, in order to provide reliable abundances, the model must fit the observed line ratios perfectly, which is by no means an easy task. Also, the observing conditions must be correctly simulated before comparing theoretical line ratios to observed ones. For example, if the

observations are obtained through a slit that covers only a small fraction of the face of a nebula, one must compute the theoretical intensities as seen through such a slit.

The results from photoionization models are strongly dependent on the assumed spectral energy distribution (SED) of the ionizing star. The latter is often assumed to be a free set of parameters in the modeling procedure. However, in some cases, spectral observations of the central star exist, and allow one to perform a direct analysis of the properties of the stellar atmosphere (effective temperature, gravity, chemical composition) by comparing the observed stellar line shapes and intensities with those produced by a tailored stellar atmosphere model.

While many detailed models of planetary nebulae or of PNe central stars have been constructed separately, there are only a few examples of studies combining both aspects (Ercolano et al. 2004; Wright et al. 2007) and for example comparing the abundances determined for the star and the nebula.

In this paper, we present such a study for IC418, an ellipsoidal PN of high surface brightness and low excitation. Its rather simple morphology combined with the impressive amount of observational material make this object an ideal test-case for a detailed combined model, associating up-to-date photoionization and atmosphere modelling codes.

This paper is structured as follows: a first section is devoted to the description of the observation material. The second sec-

tion describes the stellar and nebular modeling tools, as well as the stellar and nebular modeling process and the interactions between the two. In the third section, we present the results of our best model. In the fourth section, we discuss the expected accuracy of our results. In the fifth section, we discuss some implications from our findings, the most outstanding aspect being the comparison between stellar and nebular abundances.

2. Observations

2.1. Stellar observations

The spectrum of the central star were obtained from several sources. The data from 900 to 1100 Å were taken from FUSE observations obtained during the program P115 (PI J.M.Shull). A STIS/HST spectrum (dataset o52902) covers the range from 1190 to 1700 Å and finally we combined the IUE spectra SWP37770, SWP37773, SWP37776, SWP37778, SWP37779, SWP37783, SWP37784, SWP37785, SWP37786, SWP37792 to extend the UV spectrum to 1900 Å. The existing high resolution LWP spectra are too noisy for detailed analysis. The photometric calibration of high resolution spectra were not very reliable, so we used two low resolution IUE spectra, SWP03178 and LWR03390, in order to compare the observed and calculated stellar absolute flux.

In addition to the UV spectrum, we used a high resolution ($R \sim 20000$) optical spectrum of the central star obtained at the National Astronomical Observatory in San Pedro Martir (Mexico) using the REOSC echelle spectrograph. After the standard reduction performed with ESO-MIDAS¹, we extracted two nebular spectra in windows close to the star and with the same size. These spectra are averaged, scaled and subtracted from the stellar spectrum. In that way, all but the strongest nebular lines were removed. Due to the wind velocity of ~ 500 km/s, $H\alpha$ is broader than the nebular lines and after the subtraction of the nebula its wings were clearly seen and we use them in the following analysis.

The central star of IC418 is a known irregular variable with two characteristic timescales, one of few hours and one of few days (Handler et al. 1997). The same authors report amplitudes of 0.1 mag in V and a very small amplitude in B-V. Mendez et al. (1986) observed variations in the equivalent width of C IV 5808,12Å absorption lines on the short timescale. The time scale of the rapid variability is shorter than the wind crossing time and it is filtered by it. In fact Patriarchi & Perinotto (1995) analyzed several IUE spectra and concluded that the star does not show any detectable variability of the UV lines formed in the wind. These results means that the variability is principally related to the stellar photosphere. In the analysis presented below, we used mainly lines formed in the wind. Based on the small amplitude of the changes in brightness and color and the insensitivity of the P Cyg profiles, we conclude that the stellar variability will not affect significantly the results of the model presented in this paper.

2.2. Nebular observations

The CTIO 0.9m telescope observations obtained in 1980-1981 with the Harvard spectral scanner were taken from Gutiérrez-Moreno et al. (1985). The Lick observatory observations (1991-1992) have been reported by Hyung et al. (1994).

High spectral resolution spectra showing the emission line profiles were taken from Gesicki et al. (1996).

A deep optical echelle spectrum of IC 418 obtained in 2001-2002 at the 4m Blanco CTIO telescope is described by Sharpee et al. (2004) who measured 807 emission lines, of which 624 have been solidly identified using EMILI software (Sharpee et al. 2003).

The HST WFPC observations were obtained from the database archive (proposal 8773, Hajian). Images in the $H\alpha$, [N II] 6584Å, and [O III] 5007Å filters were used.

IC 418 was observed in the UV by the International Ultraviolet (IUE) and the IR by the Infrared Space Observatory (ISO). We take the line intensities corrected for extinction from Pottasch et al. (2004).

The UV to optical normalization was obtained following Pottasch et al. (2004), using the [O II] 2471/7325Å line ratio. We use the theoretical value given by the model (namely 0.75), taking into account the difference in the aperture sizes between the optical and UV observations. The optical values used for this calibration are the ones observed by Sharpee et al. (2004). At the end of the convergence process, we check that the absolute fluxes are reproduced.

To connect the intensities observed by ISO to the optical intensities, we use the Balmer and Brackett hydrogen lines. These lines have been observed with the ISO SWS spectrometer, while the lines of wavelength larger than 50 μ m have been observed by the LWS spectrograph. Since both spectrometers have aperture sizes larger than the entire nebula, no differential aperture correction are needed. This is confirmed by the fact that the continuum emission (supposed to arise from the external dust around the ionized nebula) has very similar intensities when observed by both spectrometers in the common wavelength range (around 45 μ m).

Notice that the absolute fluxes predicted by the model for [O II] 2471Å, the Brackett, and the Balmer lines are in a very good agreement with the observations, meaning that the calibrations we use to connect the IR, optical and UV observations are close to the absolute calibration.

The sizes and positions of the apertures used by Sharpee et al. (2004) and Hyung et al. (1994) are taken into account, as described in Sec. 3.2.

Gutiérrez-Moreno et al. (1985) report observations in the lines of [Ne v] 3425Å, [Ar v] 7006Å and He II 4686Å. We use the atmosphere model to verify whether the He II 4686Å line could be of stellar origin. The [Ne v] 3425Å and [Ar v] 7006Å are not emitted by either the star or by the nebula.

3. The models

3.1. Stellar Model

One of the major problems in building any photoionization model of a PN, apart from the density distribution (discussed in Sec 3.2), is the description of the ionizing spectrum. By definition, the photons able to ionize the gas are never observed, and the simplest hypothesis is to use a black-body distribution, defined only by an effective temperature and scaled by a luminosity. In an effort to better understand the ionization state of the nebula and to resolve some discrepancies between the model predictions and the observations, we will use a more realistic description of the ionizing flux by modelling in detail the atmosphere of the ionizing star.

The stellar atmosphere model is obtained using the CMFGEN code from Hillier & Miller (1998). CMFGEN is a

¹ <http://www.eso.org/sci/data-processing/software/esomidas/>

non-LTE line blanketed code designed for spectral analysis of stars with winds. The radiative transfer equation is solved in the co-moving frame under the restrictions of statistical and radiative equilibrium. The code is capable of treating a large number of ions with a huge number of individual levels. As a result, the emitted spectrum is reliable in a wide range of frequencies including the flux above 13.6 eV, that is responsible for the ionization of the nebula.

Contrary to other models of the star, the effective temperature is fixed not by stellar lines but using the ionization balance of the nebula. Once the ionization of the nebula is reproduced, then we check the temperature structure of the wind using the lines of N III, N IV and N V, and C III and C IV. In that way, the stellar model is consistent with the nebular model. It reproduces correctly the stellar flux bluer than the H ionization edge, which is not seen by the observer but affects strongly the nebula.

The density structure of the wind is set by an ad-hoc velocity law in the form (Hillier et al. 2003)

$$v(r) = \frac{V_{phot} + (V_{\infty} - V_{phot})(1 - R_{star}/r)^{\beta}}{1 + (V_{phot}/V_{core} - 1) \exp(-(r - R_{star})/h)} \quad (1)$$

where V_{core} define how deep the model extends and V_{phot} governs the match between the hydrostatic atmosphere and the wind. The scale factor h is defined as

$$h = \frac{kT(1 - \gamma)}{g(1 - \Gamma)\mu m_{\mu}} \quad (2)$$

where γ is the mean number of electrons per atom, $\Gamma = g_{rad}/g$ is the ratio of the radiation pressure and the gravity accelerations, μ is the mean atomic weight and m_{μ} is the atomic mass unit.

The $V_{\infty}=400$ km/s is set by the blue wings of *all* UV P Cyg profiles. For the C IV 1548,50Å lines we fit the bluest part of the saturated absorption component (some time called V_{black}) instead of the point where the blue wing rich the continuum (called V_{edge}). V_{edge} is usually affected by the velocity dispersion in the wind and can be bigger than V_{black} by 200-400 km/s. The model with derived value of V_{∞} , although smaller (by a factor of two) than the previous studies (Mendez et al. 1988; Kudritzki et al. 1997; Pauldrach et al. 2004), reproduces in detail a large number of lines. We attribute the discrepancy with other models to the better quality of the spectra (mainly FUSE and HST/STIS) used in this work, which was not available at the time of the previous studies.

Once the terminal velocity was fixed, we determine the value of $\beta = 3.0$ by fitting the width of He II 4686Å (Fig. 2). The value of h (and therefore $\log g$) were determined by fitting the wings of H γ . Fig. 1 shows the comparison between our model with $h = 0.025R_{\odot}$ which corresponds to $\log g = 3.55$ and the observed H γ wings. We use a turbulent velocity of 10 km/s during the modeling and then broaden the calculated spectrum with 30 km/s rotational velocity in order to fit the absorption lines observed in the UV spectrum.

Table 1 summarize the obtained parameters.

With wind parameters fixed we determine the abundances of the main elements. The mass loss rate and the He/H ratio is determined simultaneously from the fit to the H α , He I 5876Å, and He II 4686Å lines (Fig. 2). It was shown (Prinja et al. 2007) that P V 1117,28Å is sensitive to the wind clumping factor. The assumed clumping factor, $f = 0.1$, reproduces the profile of this line well so we do not adjust it during the fitting procedure. The Carbon abundance is measured from the fit of C III 1178Å, C III

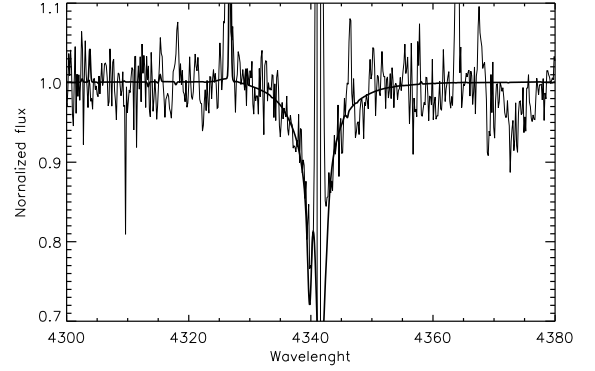


Fig. 1. Comparison between observed wings of H γ (thin line) and the model with $\log g = 3.55$ (thick line)

1247Å and C IV 1169Å lines (Fig D.3). The Nitrogen abundance is determined from the N III 1750Å, N IV 1718Å lines (Fig. D.1, Online material). The Oxygen abundance is set by O IV 1339,41Å and O III 1150Å, O III 1151Å, O III 1155Å lines (Fig. D.2, Online only). The ratios of the lines of different ionization stages of He, C and N agree with the temperature determined by the nebular response. But the observed lines of the three ionization stages of oxygen requires temperature ~ 2000 K higher. On the other hand, the FUSE spectrum of IC418 shows strong O VI 1031,37Å emission (Fig. D.2), which points to the presence of a super-ionization effect, that most probably affects all the oxygen ionization stages (Macfarlane et al. 1994). We fixed the oxygen abundance by a compromise between O III and O IV lines, expecting that the superionization effect will have less influence on these ions. In addition, the oxygen abundance affects the intensity of He II 4686Å indirectly. The assumed oxygen abundance is consistent with He II 4686Å intensity. As a result, we assign a higher uncertainty of the oxygen abundance.

The effect of superionization on the wind structure is unclear. Macfarlane et al. (1994) showed that the presence of X-ray emission can alter all the ionization stages of most of the important ions. On the other hand, the existing X-ray observations of IC418 did not show a point source. We know that some superionization exists only by the presence of O VI 1031,37Å. This problem has no simple solution, so we left its detailed study for a subsequent paper. The presence of additional ionization which is not taken into account in the model converts all the abundances obtained from the model into lower limits.

The Phosphorus abundance is determined from P V 1117,21Å, the Silicon abundance comes from the Si IV 1392,1402Å and Si IV 1122Å lines, the Sulfur abundance from S V 1502Å (Fig. D.4) and several other FUV lines and, finally, the Argon abundance is determined by Ar V 1346Å (Fig. D.2). The Iron abundance is measured by fitting the iron lines between 1250 and 1500 Å. The strong lines are usually fitted reasonably well, but there are a large number of weak lines, some of which are overestimated and some are underestimated. We attribute these discrepancies to the incorrect oscillator strengths. The neon abundance cannot be determined due to the absence of observable lines. We set its abundance to its solar value. The abundance of each element is first determined by the lines mentioned above and then checked with all other lines present in the observed spectra.

The parameters of the model that reproduces both the nebular and the stellar spectra are presented in Sect. 4.

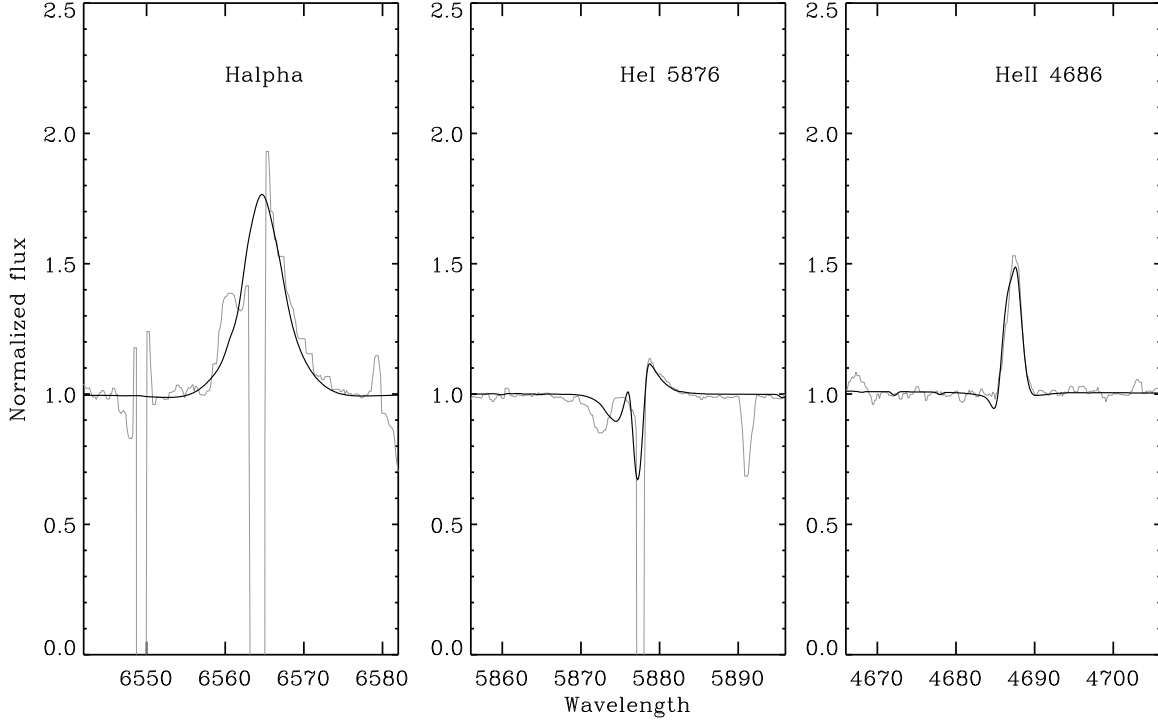


Fig. 2. The fit to the $H\alpha$, He I 5876Å, and He II 4686Å lines determines the mass loss rate and the helium abundance. Observations are plotted in gray, the model is in black. The absorption component to the blue of He I 5876Å disappears in a spectrum taken 3 days later. The lines are saturated in the spectrum and their subtraction is incorrect. The nebular subtraction removes correctly the weak lines so we expect that the oversubtraction of the saturated $H\alpha$ and N II line won't affect the wings of the stellar $H\alpha$, which were used in the analysis.

We stress that one cannot obtain a unique solution for the stellar luminosity by fitting only the normalized stellar spectrum. The parameters describing the star are not independent. If the star is described as an opaque nucleus with radius R_* and temperature T_* embedded in the wind then the luminosity is $L = 4\pi\sigma R_*^2 T_*^4$. The effective temperature T_{eff} is defined as the wind temperature at a radius where the Rosseland optical depth, τ_{Ross} , reaches 2/3. It is known (Schmutz et al. 1989), that models with the same temperature T_* and the same transformed radius

$$R_t = R_* \left(\frac{V_\infty/2500}{\dot{M}/10^{-8}} \right)^{2/3}, \quad (3)$$

have very similar emitted spectra. Substituting for the radius R_* one obtains a scaling rule for the mass loss rate.

$$\frac{\dot{M}_1}{\dot{M}_2} = \left(\frac{L_1}{L_2} \right)^{3/4}. \quad (4)$$

This means that an increase of the luminosity L can be compensated by increasing radius R_* and increasing \dot{M} . There is no easy way of removing this degeneracy except by knowing the distance. In Sec. 5.4 we discuss one method of deriving the distance. Notice that we also take into account the presence of X-ray emission in the modeling of the ionizing SED. This component doesn't have an important effect on the determination of the main parameters of the star or the nebula, thus this part is discussed in the Appendix A.

3.2. Nebular Model

The models presented in this paper are obtained using Cloudy_3D (hereafter C3D), described in Morisset (2006). We choose to use a 3D description of the object in order to take into account the different sizes and positions of the apertures used by various authors and with which we compare the model. C3D is an IDL (ITT) library of routines based on Cloudy (Ferland et al. 1998), which produces a pseudo-3D photoionization model by running several radial 1D models with the code Cloudy. In the present paper, we use version c07.02.01 of Cloudy. Each run of Cloudy corresponds to a given radial direction from the star, the input parameters being changed to reflect the geometry (inner radius, radial position of the two shells, hydrogen density). The 3D nebula is then obtained by interpolation of the results of the 1D runs, leading to a cube of physical parameters (electron temperature, ionic abundances) and emissivities of the lines of interest. More details about C3D can be found in Morisset (2006).

Notice that the apparent granularity of the nebula as seen on HST images only consists of variations of 10% in the surface brightness, that could be due to variations of 5% in the density. These small variations don't have any effects on the determination of the global properties of the nebula and we neglect them by using a smooth density distribution.

From the images of IC418, we make the hypothesis that the nebula is axy-symmetric, with a 3D distribution of the ionized gas that follows an ellipsoidal shape. The nebula is not supposed to have an inclination angle (that is: the axis of symmetry is in the plane of the sky). This rather simple morphology allows us to obtain complete models with only 4 runs of Cloudy covering polar angle between 0 and 90 deg. Due to the polar-axial

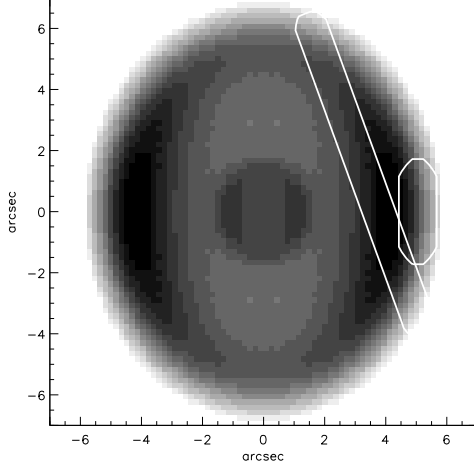


Fig. 3. Apertures used to reproduce observations by Sharpee et al. (2004) (left one) and Hyung et al. (1994) (right one), superposed upon the $H\beta$ model image.

and equatorial-planar symmetries of the nebula, only 1/8 of the whole object needs to be computed by interpolation. We use a cube of 40^3 pixels, the whole nebula being obtained by merging the same cube after adequate rotations, leading to a 80^3 pixels cube.

Emission line maps are then obtained by summing up the emissivity cube among a given direction (small axis in our present case). To compare with the observed line intensities, the slit sizes and positions are also needed. Some of the optical observations have been obtained through apertures smaller than the whole object (Hyung et al. 1994; Sharpee et al. 2004). In the following, we will apply the same aperture sizes, orientations and positions to the emission line intensity maps when comparing with these author's line intensities, while the full object is taken into account for the UV and IR intensities. Fig. 3 shows the apertures used. Notice that from the models described below, we found that only 10% (3.5%) of the $H\beta$ flux is intercepted by the optical aperture used by Sharpee et al. (2004) (Hyung et al. 1994, resp.).

The set of free parameters needed to fully describe a model and compare it to the observations is the following: the 3D density distribution, the angular size of the nebula (or its distance), the nebular abundances, the ionizing photons distribution and the number of ionizing photons emitted per time unit (Q_0). The processes to determine the adopted values for these parameters are described in the following subsections.

The morphology of IC418 was obtained by trial and error, using the HST images of $H\beta$, [O III] 5007Å and [N II] 6584Å and density diagnostics (11 line ratios).

The main goal in the determination of a somewhat complex density distribution is to reproduce the central enhanced emission from [O III] 5007Å. This is reached by using a double ellipsoidal shell morphology, where the density is adjusted to reproduce the emission line diagnostics. The exact density distribution cannot be achieved without a high resolution density map, as for example given by a [S II] 4068/4076Å map. Nevertheless, the density distribution obtained here is constrained sufficiently by the overall density diagnostics and the surface brightness maps.

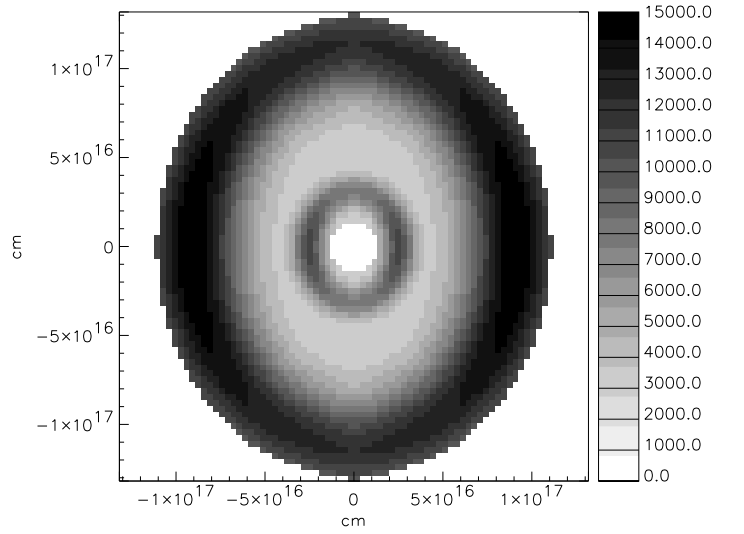


Fig. 4. Cut in the density distribution through a plane including the polar axis, units in cm, gray-scale in hydrogen atom/cm³.

The adopted density distribution consists of two ellipsoidal shells of distinct densities, sizes and widths. Its analytical description in a spherical coordinate system is the following:

$$\begin{aligned} n_H(R < R_{in}) &= 0, \\ n_H(R > R_{in}, \theta) &= n_0 + \\ &\quad n_1(\theta) \times \exp\left(-\left(\frac{R-R_1(\theta)}{\sigma_1}\right)^2\right) + \\ &\quad n_2(\theta) \times \exp\left(-\left(\frac{R-R_2(\theta)}{\sigma_2}\right)^2\right), \end{aligned} \quad (5)$$

with an angular dependence of the parameters as follows:

$R_1(\theta) = R_1 \times F_{ell-1}(\theta)$, $R_2(\theta) = R_2 \times F_{ell-2}(\theta)$, $n_1(\theta) = n_1 / F_{ell-1}(\theta)$ and $n_2(\theta) = n_2 / F_{ell-2}(\theta)$, where θ is the polar angle (set to 0 in the equatorial direction), and $F_{ell}(\theta)$ is an ellipsoid magnification factor defined by:

$$F_{ell-i}(\theta) = a_i / \sqrt{(\sin(\theta))^2 + (a_i \times \cos(\theta))^2},$$

where a_i is an adimensional coefficient, set to 1.3 ($i=1$) and 1.5 ($i=2$) for the inner and outer ellipse respectively. Numerical values for these parameters for the best fit we obtain are given in Table 1, see below.

The Figure 4 shows the hydrogen density distribution in a plane containing the polar axis of symmetry. The full density distribution is obtained by rotation about the polar axis. We will use this density distribution for the model presented in the following sections.

Fig. 5 show $H\beta$, [O III] 5007Å and [N II] 6584Å images of the nebula, and the ratios of these lines, for both the HST observations and the model respectively. The curves are $Y=0$ arcsec cuts in the surface brightness, passing through the central point. In the case of the HST images, the central star emission has been removed to allow better comparison between the model and the observed images. The global shape of the nebula is well reproduced by our model.

The flat top of the [N II] 6584Å image is due to saturation effect of observation. We artificially saturate the model image

taking the same ratio between the mean value at the center of the image (without the star) and the saturation value. The resulting saturated profile is shown with a thicker line, reproducing the observed profile.

With the density distribution determined, we run models with the stellar SED determined in Sec. 3.1. The abundances of the elements are then determined by fitting the most important lines of all the observable ions for each element. A total of 140 emission lines are used for the model, most of them being pure predictions (not used for the convergence process). The complete process of convergence is achieved by fine tuning the effective temperature until we successfully reproduce the ionization state of the nebula, once the $H\beta$ absolute flux is well reproduced.

The ISO observations show a continuum emission, commonly associated with dust. The emission reaches a maximum value of 400 Jy close to 35 μm . It is out of the scope of the present paper to reproduce the exact shape of the dust emission. Nevertheless we do include dust in the photoionization model to take into account its absorption when fitting the stellar continuum and determining the interstellar extinction. We check that the dust emission is globally of the order of the observation.

4. Presentation of our best model

4.1. Parameters of the nebular and stellar models

The parameters for the adopted model are described in Table 1. Table 2 lists the abundances for the adopted models (stellar and nebular) and from the literature (for the nebula). These abundances by mass (for the model and the literature) are also presented in Fig. D.8 (Online only). Notice that our values for C/H, N/H and O/H are comparable to the largest values obtained previously, which also correspond to the more recent determinations (namely Pottasch et al. 2004; Sterling et al. 2007).

4.2. Comparing the stellar parameters with previous studies

Stellar models of the central star of IC418 are available in the literature: Mendez et al. (1988); Kudritzki et al. (1997); Pauldrach et al. (2004). The stellar parameters obtained by these authors and in this work are summarized in the Tab 3. In general the parameters obtained in this paper are similar to the once obtained by other authors although the values presented here have the advantage to be consistent with the nebula and the evolutionary status of the star. Our value of V_∞ reproduce most of the features in the observed spectrum especially the FUV lines which were not available at the time of previous modeling. In general one can conclude that the parameters obtained here are compatible with the previous values and the main contribution of this paper is the more reliable auto consistent values and chemical composition of the star.

4.3. Defining tolerance and quality factor $\kappa(O)$ to compare the nebular model and the observations

To compare the results of the model to the observations, we define errors in the observed intensities, $\frac{\Delta I}{I}$, as the following: 10% for lines brighter than 0.1 $H\beta$, 20% for lines between 0.01 and 0.1 $H\beta$, 30% for lines lower than 0.01 $H\beta$. To take into account the lowest signal/noise ratio for the IUE and ISO observations and the uncertainties in the connection between the optical and the IR and UV domains, we add 20% to the previously determined errors for the IR and UV lines. We also add 10%

Table 1. Parameters of the model.

Parameter	Unit	Adopted model
Teff	kK	36.7
$\log(Q_0)$	s^{-1}	47.5
$\log(L)$	L_\odot	3.88
$\log(g)$		3.55
V_∞	km.s^{-1}	450
Mdot	$10^{-8} M_\odot.\text{yr}^{-1}$	3.6
Nucleus Mass	M_\odot	0.6
Teff(X)	kK	290
$\log(L(X))$	L_\odot	0.5
n_0	cm^{-3}	2700
n_1	cm^{-3}	7500
n_2	cm^{-3}	11700
$\langle n \rangle$	cm^{-3}	9300
$\log(R_{in})$	cm	16.09
$\log(R_1)$	cm	16.16
$\log(R_2)$	cm	16.96
$\log(\sigma_1)$	cm	16.
$\log(\sigma_2)$	cm	16.5
$f f_c$		1.
Distance	kpc	1.26
Age	a	1400
H^+ mass	M_\odot	0.06
T0	K	8575
t^2		0.002
$T(O^+)$	K	8690
$T(O^{++})$	K	8375
$T(N^+)$	K	8810
$T(N^{++})$	K	8375

for the optical lines obtained by Gutiérrez-Moreno et al. (1985); Hyung et al. (1994). Notice that these errors also aim to take into account the numerical and modeling uncertainties due to the limited complexity of the morphology we adopt, the errors in atomic data we use, and the effects of the position and size of the apertures we use (see the comments about rotating apertures during the observations by Hyung et al. (1994)).

A quality factor for the fit of an observable is defined by

$$\kappa(O) = (\log O_{\text{mod}} - \log O_{\text{obs}}) / \tau(O), \quad (6)$$

where O_{mod} is the value returned by the model, O_{obs} is the observed value, and $\tau(O)$ is the accepted tolerance in dex for this observable. We define a tolerance as $\tau(O) = \text{Log}(1 + \frac{\Delta I}{I})$. When the absolute value of $\kappa(O)$ is lower than 1, the model value is within the adopted tolerance of the observed value. The value of $\kappa(O)$ is also used to analyse the diagnostic line ratios.

4.4. Line ratios and absolute fluxes

Table 4 presents the intensity ratios obtained for our best model and compares them with the observed values. Some lines appear more than once because they have been observed by various authors and through different apertures. The second column gives the reference for the observation. The third and fourth columns are the observed values and the result of the model, respectively. The fifth column is $\kappa(O)$, the quality factor of the fit, as defined in Sec. 4.3. Figure 6 shows all the values of $\kappa(O)$ versus the ionization potentials (IPs) of the ions giving rise to the lines. Horizontal lines at $\kappa(O) = \pm 1, \pm 2$ help to see the lines that are fitted within an acceptable tolerance.

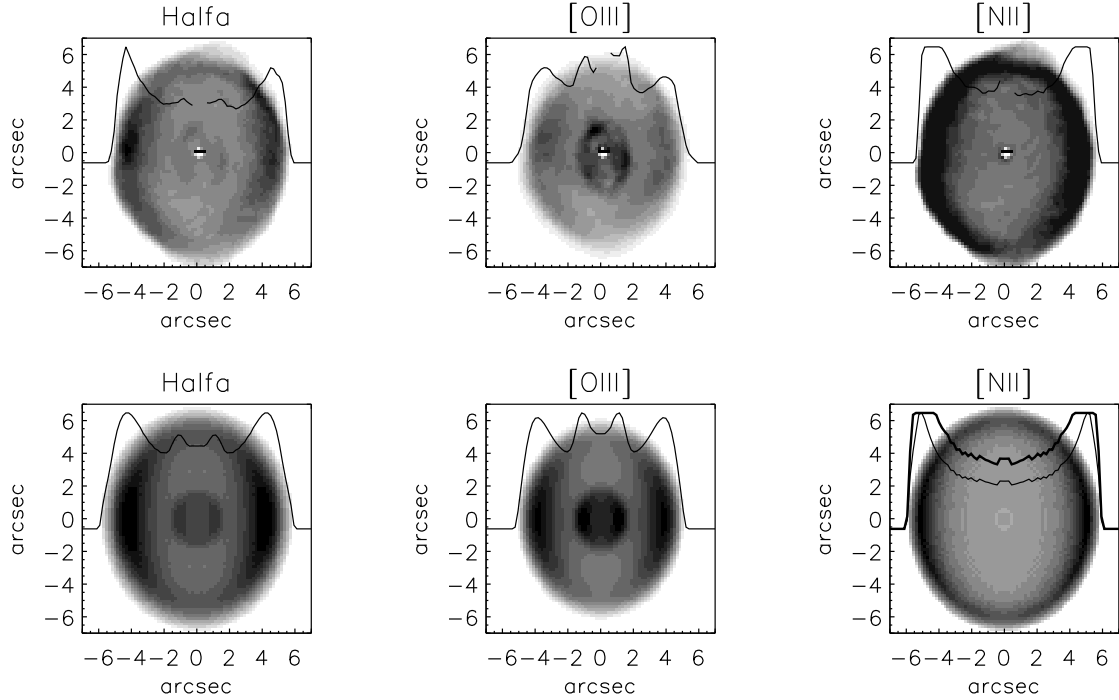


Fig. 5. We compare the HST images (top) and the model images (bottom) for 3 emission lines. Units are arcsec. Gray values are linear arbitrary scale. The lines are $Y=0$ arcsec cuts in the surface brightness maps.

Table 2. Abundances from the literature and for the adopted model

	He	C	N	O	Ne	Mg	Si	P	S	Cl	Ar	Fe
BY NUMBER in log												
Best Stellar Model	-0.60	-3.30	-4.24	-3.42			-4.29	-7.11	-5.36		-5.29	-4.74
Best Nebular Model	-0.92	-3.10	-4.00	-3.40	-4.00	-4.95	-4.90		-5.35	-7.00	-5.80	-7.40
LITERATURE NEBULAR ABUNDANCES (BY NUMBER in log)												
Sterling et al. (2007) Model A	-0.975	-3.22	-3.97	-3.29	-3.99				-5.40	-7.07	-5.79	
Sterling et al. (2007) Model B	-0.850	-3.32	-3.97	-3.43	-3.75				-5.35	-7.11	-5.81	
Pottasch et al. (2004)	-1.142	-3.21	-4.02	-3.46	-4.05				-5.36	-6.92	-5.74	
Henry et al. (2000)	-1.066	-3.66	-4.07	-3.81	-5.02							
Hyung et al. (1994) Model	-1.155	-3.52	-4.15	-3.74	-5.52	-5.55	-6.00		-5.60	-7.00	-6.26	
Hyung et al. (1994) ICF	-1.155	-3.57	-4.08	-3.67	-4.22	-5.16			-5.56	-7.11	-5.72	
Aller et al. (1980)	-0.920	-3.22	-4.22	-3.37	-4.40				-5.38	-6.85	-5.34	
Aller & Czyzak (1983)	-1.030	-3.21	-4.13	-3.36	-4.13				-5.38	-7.06	-5.64	
Beck et al. (1981)					-4.12				-5.21		-5.74	
Buerger (1973)	-0.796	-3.70	-4.40	-3.60	-4.50				-5.00	-6.82	-5.30	
Solar (Asplund et al. 2005)	-1.070	-3.61	-4.22	-3.34	-4.16	-4.47	-4.49	-7.00	-4.86	-6.50	-5.82	-4.55
BY MASS in log												
Best Stellar Model	-0.30	-2.52	-3.40	-2.52			-3.15	-5.92	-4.16		-3.99	-3.30
Best Nebular Model	-0.49	-2.20	-3.03	-2.37	-2.88	-3.75	-3.63		-4.02	-5.63	-4.37	-5.83
Solar (Asplund et al. 2005)	-0.60	-2.66	-3.21	-2.27	-2.99	-3.22	-3.17	-5.28	-3.49	-5.09	-4.35	-2.93

Figure 7 shows the distribution of the values of $\kappa(O)$. The symbols are related to the emitting element. Most of the values of $\kappa(O)$ are in the $[-1,1]$ range, that is, the value obtained by the model agrees with the observed one within tolerances.

We do not see a larger discrepancy between the model predictions and the observed intensities for lower intensities. We interpret this as an indication that the tolerances defined in Sec.4.3 are adequate.

The Hydrogen recombination lines are almost all well reproduced, with the notable exception of $H\alpha/H\beta$, for which the observed values are 3.5 and 3.1, considerably higher than the predicted value of 2.9. We can suspect this is an observational problem.

The Helium recombination lines are also mostly fitted within the tolerance. When a given line is not fitted (e.g. $He\text{ I }5876$), it's only the case for one observation of the given line, the other ob-

Table 3. Stellar parameters from the literature and for the adopted model

Reference	$\log(L/L_\odot)$	T(kK)	$\log g$	M/M $_\odot$	d(kpc)	\dot{M} (10 $^{-7}$ M $_\odot$ /yr)	V $_\infty$	R/R $_\odot$
Mendez et al. (1988)	4.2	36.	3.3	0.77	2.0			3.25
Kudritzki et al. (1997)	4.3	37	3.3	0.89		2.6	700	3.5
Pauldrach et al. (2004)	4.2	39	3.7	1.33	2.0	0.72	800	2.7
This work	3.88	36.7	3.55	0.60	1.26	1.1 ^a	450	2.17

a) Value of smooth wind which correspond to 3.6×10^{-8} M $_\odot$ /yr with clumping factor $f=0.1$.

servations of the same line are well reproduced ($\kappa(\text{He I } 5876\text{\AA}) = -1.74, -1.09, 0.47$ depending upon the observation).

The 3 most intense lines of Carbon are reproduced within the tolerance.

The [N II] 6548, 6584Å lines are reported by 3 authors, the resulting 6 observed intensities are well reproduced with a mean $\kappa(\text{[N II] } 6548, 6584\text{\AA})$ of 0.13. Notice the very small value predicted for [N I] 5200Å, 8 times smaller than the observation. A discussion of the electron excitation collision strengths of N⁺ can be found in Péquignot et al. (2001) who questioned the values published by Tayal (2000), but the version of cloudy we used (namely c07.02.01) takes the collision strengths from Tayal (2006) which are supposed to be 20 times greater at electron temperature of about 8000 K. This line is emitted by the very external part of the nebula. Any small variation in the position of the slit or the external electron density could strongly affect the prediction.

The O I lines are globally predicted half the observed values. They are also emitted close to the edge of the nebula and the same considerations as for [N I] lines about the slit position apply. The [O II] lines are well reproduced, with the exception of the [O II] 3726, 3729Å observed by Sharpee et al. (2004), predicted 40% lower than observed. On the other hand, the observed intensities for the same lines reported by Hyung et al. (1994) are reproduced 25% higher than observed. The [O II] 7320, 7330Å lines are better reproduced, with the same tendencies. The [O III] 4959, 5007Å lines are reported by 3 authors, the corresponding 6 intensities are reproduced with a mean $\kappa(\text{[O III] } 4959, 5007\text{\AA})$ of 0.6. The observed value for [O III] 5007Å/H β is ranging from 0.86 to 2.1 depending on the author. The values predicted by the model are ranging from 1.1 to 2.0, clearly showing the effect of changing the position and size of the aperture and the need of taking it into account in the fitting process.

The 5 values reported in the literature for the [Ne III] lines are reproduced with a mean value for $\kappa(\text{[Ne III]})$ of -0.6, while $\kappa(\text{[Ne II] } 12.8\mu\text{m}) \sim 0.5$.

The 10 values reported for the [S II] lines are reproduced with a mean $\kappa(\text{[S II]})$ of -0.12, while we found a mean $\kappa(\text{[S III]})$ of 0.46, using 9 lines of [S III]. The mean value of $\kappa(\text{[Cl II]})$ is -0.52 (5 lines) and the mean value of $\kappa(\text{[Cl III]})$ is -0.24 (9 lines). For the Ar lines, the mean value for $\kappa(\text{[Ar III]})$ is 0.10, based on 8 lines.

All these mean values for $\kappa(\text{O})$ are indicative only, as some very faint lines can enter in the mean and dominate it. Fig. 6 is very instructive to get an idea of the global quality of the fit. Notice that for Mg and Si only one line of each element is detected.

Some lines are permitted lines that are suspected to have a strong fluorescence contribution, and for which $\kappa(\text{O})$ is much lower than -1 (See Escalante & Morisset 2005, for the NII fluorescence spectrum). They are designed by an ^a close to the wavelength. For example, the N III 4641Å line is virtually not

produced by recombination of the N⁺⁺⁺ ion (requiring 47 eV photons), but rather is emitted entirely by fluorescence, implying that the N⁺⁺ ion is responsible for the emission.

Table D.1 (Online only) compares the observed electron density and temperature diagnostics with the results from the model. These results are also plotted in Fig. 8. From the 11 density diagnostics that are available from the observed line ratios, we find a very good agreement between the model and the observed values. The only value of $\kappa(\text{O})$ that is not in the [-1,1] range is [Ar IV] 4740/4711Å, perhaps indicating the presence of a slightly higher density thin shell or clumps close to the star. The mean value of $\kappa(\text{density diagnostics})$, without taking into account the [Ar IV] 4740/4711Å ratio, is 0.12.

21 diagnostic line ratios are available for the electron temperature, and most of them show a good agreement between the observed ratios and the results of the model. We nevertheless notice the disagreement for the low ionization species (S II and Cl II). The extreme value of 3.1 is obtained for $\kappa(T_e(\text{[O II] } 7320/3727\text{\AA}))$ for the Sharpee et al. (2003) observation. On the other hand, for the same diagnostic ratio using Hyung et al. (1994) observations, we find $\kappa(\text{O}) = -0.2$. This demonstrate the difficulties of the fitting exercise, especially when relying on a unique set of observations. The same apply for the classical $T_e(\text{[O III] } 5007/4363\text{\AA})$ diagnostic, rather well reproduced when comparing to the Sharpee et al. (2003) observations, but less well fitted if using the Hyung et al. (1994) or Gutiérrez-Moreno et al. (1985) observations. For most of the diagnostics for which we have $|\kappa(\text{O})| > 1$, there is another observation of the same diagnostic for which $|\kappa(\text{O})| < 1$. See Sect. 5.1 for a discussion of the small discrepancy between the model and the observed electron temperature diagnostics.

Figure D.5 (Online only) shows that there is no systematic trend for $\kappa(\text{O})$ as a function of either the wavelength (upper panel) or the critical density of the forbidden lines (lower panel). The first result indicates that there is no important error in the reddening correction applied to the emission line intensities. If there is a low density inter-clump medium, it could be detected by low critical density lines. The absence of a clear trend in the lower panel of figure D.5 indicates that there is no detectable low density medium : it could mean that there are no clumps at all and that the medium is rather homogeneous, or that any inter-clump medium has a very low density. See Sects 5.3 and 5.4 for a discussion of the determination of the clumping factor.

Table 5 displays the predicted absolute fluxes in the 4 lines used to cross-calibrate different spectral regimes, and the corresponding observed values. The agreement is extremely good. In this way we verify that our cross calibration between the different wavelength regions, described in Sec. 2.2, is good.

Table 4. Results of the $T_{\text{eff}}=36.7$ kK CMFGEN model. I: Line (Wavelengths in Å except for IR observations, in μm), II: Observatory: 0: CTIO (Sharpee et al. 2004), 1: ISO (Pottasch et al. 2004), 2: IUE (Pottasch et al. 2004), 3: Lick (Hyung et al. 1994), 4: CTIO (Gutiérrez-Moreno et al. 1985), III: Observed intensity (corrected for dust attenuation, with $H\beta = 100$), IV : Model, V : Quality factor $\kappa(\text{O})$ (See Sec. 4.3).

I	II	III	IV	V	I	II	III	IV	V	I	II	III	IV	V
HI 3835	0	9.490	7.841	-1.05	NI 8212 ^a	0	0.142	0.002	-16.64	[S II] 4070	0	1.780	2.313	1.44
HI 3835	3	6.950	7.829	0.45	N III] 1750	2	0.584	0.637	0.21	[S II] 4070	3	2.440	3.209	1.04
HI 3970	0	16.900	16.511	-0.24	[N III] 57.2	1	3.323	2.722	-0.59	[S II] 4078	0	0.765	0.750	-0.07
HI 3970	3	15.980	16.501	0.18	N II 4041	0	0.012	0.018	1.43	[S II] 4078	3	0.880	1.041	0.50
HI 4102	0	24.800	26.575	0.73	N II 4176	0	0.006	0.003	-3.43	[S II] 6716	0	2.080	1.863	-0.60
HI 4102	3	25.240	26.580	0.28	N II 4239	0	0.013	0.012	-0.17	[S II] 6716	3	3.590	2.501	-1.38
HI 4340	0	44.800	47.326	0.58	N II 4435	0	0.003	0.008	3.81	[S II] 6716	4	2.090	1.988	-0.19
HI 4340	3	47.000	47.341	0.04	N II 4530	0	0.004	0.004	-0.53	[S II] 6731	0	4.420	3.846	-0.76
HI 6563	0	312.000	291.434	-0.71	N II 4552 ^a	0	0.003	0.001	-2.79	[S II] 6731	3	6.790	5.174	-1.04
HI 6563	3	350.000	291.063	-1.01	N II 5495 ^a	0	0.015	0.003	-5.99	[S II] 6731	4	4.270	4.092	-0.16
HI 2.62	1	4.718	4.855	0.09	N II 5679 ^a	0	0.067	0.017	-5.32	[S III] 6312	0	0.857	0.873	0.07
HI 4.05	1	8.557	8.679	0.04	N III 4641 ^a	0	0.005	0.000	-38.03	[S III] 6312	3	0.940	0.925	-0.05
HI 7.45	1	2.731	2.815	0.09	[O I] 5577	0	0.026	0.017	-1.59	[S III] 6312	4	0.960	0.865	-0.31
He I 4026	0	2.098	2.005	-0.25	[O I] 6300	0	2.170	1.137	-3.55	[S III] 9069	0	17.800	18.799	0.57
He I 4471	0	4.490	4.280	-0.26	[O I] 6300	4	2.040	1.302	-1.71	[S III] 9069	3	14.550	18.896	1.43
He I 4471	3	3.590	3.288	-0.34	[O I] 6363	0	0.759	0.363	-2.82	[S III] 9532	0	42.200	46.621	1.04
He I 4471	4	4.170	4.116	-0.05	[O II] 2471	2	19.271	18.374	-0.18	[S III] 9532	3	38.090	46.861	1.14
He I 4713	0	0.610	0.647	0.22	[O II] 3726	0	123.800	88.632	-3.51	[S III] 18.6	1	15.204	16.078	0.21
He I 5876	0	13.670	11.557	-1.76	[O II] 3726	3	90.530	115.323	1.33	[S III] 33.4	1	2.617	2.600	-0.02
He I 5876	3	10.850	8.885	-1.10	[O II] 3729	0	52.340	34.851	-4.27	[S IV] 10.5	1	1.266	2.929	2.49
He I 5876	4	10.200	11.102	0.47	[O II] 3729	3	37.720	45.228	1	[Cl II] 8579	0	0.284	0.183	-1.69
He I 6678	0	3.870	2.960	-1.47	[O II] 7323	0	13.740	13.333	-0.32	[Cl II] 8579	3	0.270	0.248	-0.25
He I 6678	3	2.550	2.283	-0.42	[O II] 7323	3	15.680	18.152	0.80	[Cl II] 9124	0	0.077	0.048	-1.78
He I 6678	4	2.750	2.845	0.13	[O II] 7332	0	11.500	10.733	-0.72	[Cl II] 9124	3	0.050	0.066	0.80
He I 7065	0	7.040	8.266	0.88	[O II] 7332	3	13.380	14.613	0.48	[Cl II] 6162	0	0.004	0.004	0.28
He I 7065	4	5.130	7.867	1.63	O I 7773	0	0.075	0.054	-1.29	[Cl III] 5518	0	0.182	0.179	-0.05
He I 7281	0	0.791	0.683	-0.56	O I 8447 ^a	0	1.142	0.007	-28.20	[Cl III] 5518	3	0.190	0.170	-0.33
[C I] 8727	0	0.033	0.030	-0.39	O I 9264	0	0.027	0.020	-1.06	[Cl III] 5518	4	0.450	0.182	-2.69
[C II] 157.	1	1.100	0.403	-2.98	[O III] 4363	0	0.935	0.710	-1.05	[Cl III] 5538	0	0.356	0.356	0.00
C II] 2326	2	81.462	88.482	0.31	[O III] 4363	3	0.520	0.421	-0.63	[Cl III] 5538	3	0.380	0.348	-0.26
C III] 1909	2	27.592	34.878	0.89	[O III] 4363	4	0.910	0.716	-0.71	[Cl III] 5538	4	1.000	0.353	-3.09
C II 1335	2	23.212	20.164	-0.54	[O III] 4959	0	72.700	65.158	-1.15	[Cl III] 8436	0	0.006	0.010	1.68
C II 1761 ^a	2	2.102	0.349	-5.34	[O III] 4959	3	29.520	37.300	1.28	[Cl III] 8483	0	0.011	0.010	-0.29
C II 4267	0	0.570	0.452	-0.88	[O III] 4959	4	50.100	65.034	1.43	[Cl III] 8504	0	0.004	0.009	2.80
C II 4267	4	0.690	0.436	-1.36	[O III] 5007	0	214.000	196.126	-0.92	[Ar II] 6.98	1	5.997	6.184	0.09
C II 4619	0	0.011	0.021	2.61	[O III] 5007	3	85.870	112.273	1.47	[Ar III] 5192	0	0.039	0.034	-0.43
C II 6580 ^a	0	0.805	0.039	-11.52	[O III] 5007	4	151.000	195.754	1.42	[Ar III] 5192	3	0.030	0.027	-0.28
C II 7231 ^a	0	0.169	0.006	-12.66	[O III] 51.8	1	15.261	13.430	-0.49	[Ar III] 7135	0	8.260	7.736	-0.36
[N I] 5198	0	0.201	0.046	-5.58	[O III] 88.3	1	2.407	1.854	-0.77	[Ar III] 7135	3	6.180	5.937	-0.15
[N I] 5200	0	0.117	0.016	-7.69	O II 4152	0	0.018	0.023	0.88	[Ar III] 7135	4	6.030	7.417	0.79
[N II] 5755	0	2.760	2.599	-0.33	O II 4341	0	0.085	0.091	0.23	[Ar III] 7751	0	2.196	1.867	-0.89
[N II] 5755	3	3.910	3.723	-0.19	O II 4593 ^a	0	0.024	0.004	-6.37	[Ar III] 7751	3	0.780	1.433	1.81
[N II] 5755	4	2.190	2.694	0.79	O II 4651	0	0.171	0.172	0.01	[Ar III] 9.00	1	7.334	8.039	0.27
[N II] 6548	0	53.600	53.094	-0.10	[Ne II] 12.8	1	53.098	61.004	0.53	[Ar IV] 4711	0	0.003	0.003	0.08
[N II] 6548	3	71.230	73.639	0.18	[Ne III] 3869	0	3.090	2.806	-0.53	[Ar IV] 4740	0	0.004	0.005	1.58
[N II] 6548	4	51.300	54.902	0.37	[Ne III] 3869	3	2.050	1.147	-2.21	[Fe III] 4659	0	0.027	0.027	-0.06
[N II] 6584	0	162.900	156.681	-0.41	[Ne III] 3869	4	2.630	3.766	1.37	[Fe III] 5271	0	0.015	0.017	0.34
[N II] 6584	3	206.830	217.309	0.27	[Ne III] 3968	0	0.970	0.846	-0.52	[Fe III] 4881	0	0.015	0.013	-0.52
[N II] 6584	4	151.000	162.014	0.39	[Ne III] 3968	3	0.640	0.346	-1.83	Mg II 2798	2	16.351	15.697	-0.16
[N II] 121.	1	0.283	0.189	-1	[Ne III] 15.5	1	9.512	9.276	-0.08	[Si II] 34.8	1	0.936	0.985	0.13

^a Lines suspected to be mainly emitted by fluorescence.

Table 5. Comparison of some predicted and observed absolute fluxes (units in 10^{-10} erg.cm⁻².s⁻¹, except for the 6cm continuum, in Jy). The model $H\beta$ and [O II] 2471Å fluxes are reddened using $E_{B-V}=0.26$ and $R_V=3.6$. The observed (reddened) values are taken from Pottasch et al. (2004)

Line	Observation	Model
$H\beta$	2.7	2.56
[O II] 2471Å	0.24	0.21
H I 4.05 μm	.45	0.59
6 cm continuum	1.73	1.96

4.5. Fitting the IUE observations

Fig. 9 compares the observed IUE stellar spectrum with the stellar model used in the photoionization model. The model shown here is the CMFGEN star taking into account the nebular absorption and the ISM attenuation. We found that the best extinction law to reproduce the IUE observations is obtained using the Fitzpatrick (1999) law with $E_{B-V}=0.26$ and $R_V=3.6$. The 2200Å bump is reproduced, as well as the EUV ISM attenuation. This value for E_{B-V} is within the range obtained from the literature (from 0.14 to 0.37, see Pottasch et al. 2004; Sharpee et al. 2004, and references therein).

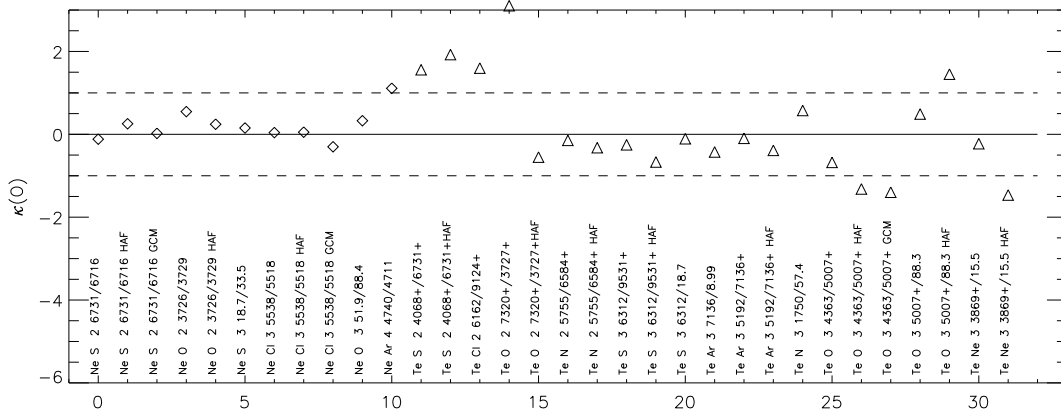


Fig. 8. Quality factors $\kappa(O)$ for the diagnostic ratios (diamonds for electron density and triangles for electron temperature) from Tab. D.1. For the optical lines, HAF refers to Hyung et al. (1994), GCM to Gutiérrez-Moreno et al. (1985), and to Sharpee et al. (2003) otherwise. Other observations are described in Sec. 2.2.

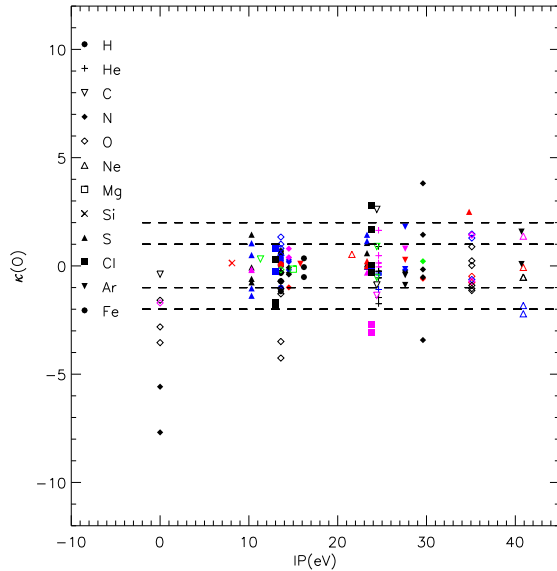


Fig. 6. Quality factors $\kappa(O)$ vs. the ionization potential of the emitting ion. Each symbol corresponds to a given element.

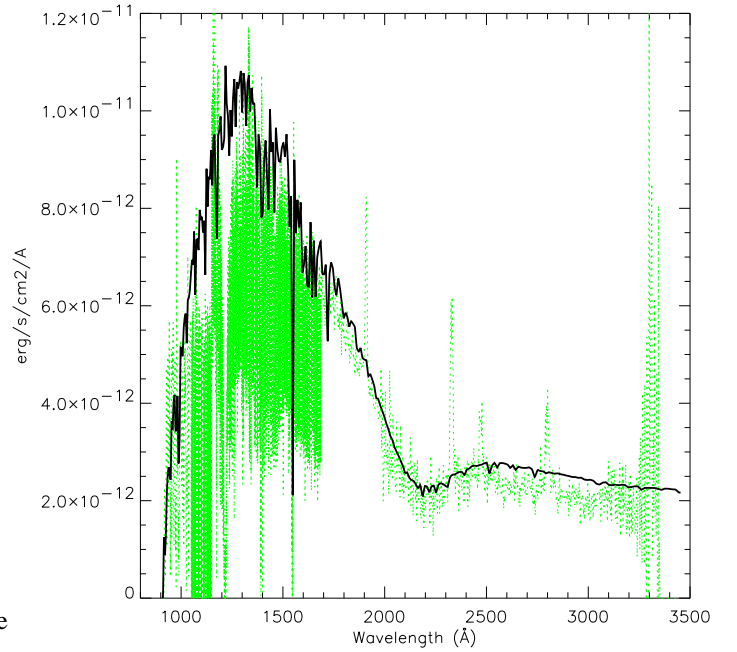


Fig. 9. Comparison between the IUE observations and the stellar SED from the CMFGEN model.

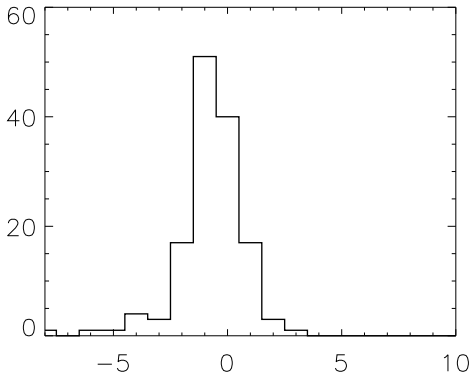


Fig. 7. Histogram of $\kappa(O)$ distribution.

5. Discussion

5.1. Missing power

We point out that, contrary to the electron density, which is an input parameter of the model (because totally controlled by the Hydrogen density), the electron temperature is an output, as it is the result of the energy balance in the nebula, and depends on the ionizing spectrum and the metals abundances. Thus the electron temperature diagnostics are predictions for the present model, because all the parameters that can have an impact on the temperature are fixed: the ionizing SED is constrained by the stellar observations and the abundances of the major coolants are controlled by emission lines that are already fitted. Even if the fits of the electron temperature diagnostic line is relatively good, the model presented here seems to be a little too cool. On the other

hand, the fit to the intensities of the collisionally excited lines is also globally a little bit low (see the distribution of $\kappa(\text{O})$ in Fig. 7). This small discrepancy between the model and the observation could be solved by adding an extra heating process.

We test a model with an extra heating value of $10^{-20.3} \times (n_H/n_0) \text{ erg.cm}^{-3}.\text{s}^{-1}$ (for this we used c08.00 version of Cloudy, with $n_0 = 1 \text{ cm}^{-3}$), to obtain electron temperature diagnostics closer to the observations. This leads to an increase of the mean electron temperature from 8575 K to 9046 K. The corresponding total additional power is $4 \times 10^{35} \text{ erg.s}^{-1}$, representing 30% (!) of the heating coming from the star (or the cooling emitted by the nebula, as they are equal by assumption of thermal equilibrium). The collisionally excited lines in this boosted model are globally closer to the observed values.

5.2. Where blackbody fails

To test the validity of using a simple SED for the ionizing flux instead of an atmosphere model, we perform a model with a blackbody (BB) distribution. We keep all the parameters at the value of the model described above, except for the stellar temperature, which is set to 39.5 kK to produce a global ionization of the nebula similar to what is obtained with the CMFGEN model. Figs. D.6 and D.7 (Online only) is similar to Fig. 6 and 7 respectively, except that they involve this BB model.

All the elements but Ne and Ar show line intensities very similar to the ones obtained with the adopted model. For Ar and Ne, the ions of high IPs > 40 eV (namely Ne^{2+} and Ar^{3+}) are strongly overpredicted by the BB model, relative to the lower IPs ions from the same species. We attribute these overpredictions to the shape of the SED at high energy (see Fig. 10). The absorption features visible between 40 and 50 eV are mainly produced by C III, O IV, and Ne III, between others.

The main difference between the BB model and the CMFGEN model is only visible above 40 eV. For energies below this limit, the two SEDs are very similar. Thus, in the absence of any atmosphere model, the Planck hypothesis is a good approximation for the ionizing flux between 10 and 40 eV, but there is a significant shift in the effective temperature (here a Planck function at 39.5 kK is similar to an atmosphere model close to 36.7 kK).

We note that Hyung et al. (1994) obtained very low abundances for Ne and Ar using a photoionization model of IC418. We suspect that the SED they used is responsible for this discrepancy with our results.

5.3. Clumping factor and distance determination

Neither the geometrical size of the nebula, the distance, nor the absolute luminosity of the central star are well-constrained. Multiplying the stellar luminosity by a factor K_1 but all the sizes of the nebula (inner radius, positions and sizes of the 2 shells) by $K_1^{1/3}$ will lead to the same position of the recombination front and then the same appearance (because the Strömgren radius is proportional to $Q_0^{1/3}$). If the distance to the observer is also multiplied by $K_1^{1/3}$, the angular size is kept constant, while the absolute luminosity (H β for example) is multiplied by the same factor $K_1^{1/3}$. On the other hand, changing Q_0 and the sizes by factors K_1 and $K_1^{1/3}$, respectively, leads to an increase of the ionization parameter $U = Q_0/(4.\pi.R^2.N_H.c) \propto K_1^{1/3}$. This will lead to an increase of the intensities of the lines emitted by high IPs ions (e.g. O III, Ar IV, Ne III) and a decrease of the intensities of the low

IPs lines (e.g. S II). This behaviour is very similar to the reaction of the nebula when the stellar temperature increases. We use the H β absolute flux to resolve the degeneracy and to fine tune the effective temperature of the star (with a latitude of 500 K, the first order value being obtained from the stellar spectrum fit) by reproducing the ionization state of the nebula.

Another factor that can strongly increase the uncertainty in the morphology (and distance) determination is the filling factor. This factor can be divided into 2 parts: a morphological filling factor ff_M and a clumping factor ff_C . The first one represents the volume of the gaseous nebula over the volume of the total extension of the nebula. In the simple case of a thin shell of external radius R_{neb} surrounding an empty cavity of radius R_{cav} , we have $ff_M = 1 - (R_{cav}/R_{neb})^3$. The use of a detailed description of the nebular density structure fixes this morphological filling factor. On the other hand, the clumping filling factor aims to take into account any possible small scale structure of the nebula, where the gas would be concentrated in small clumps. The physical process that could lead to such a situation is not clear, the real situation is certainly not clumps in the middle of vacuum, but this filling factor is often used as the first moment of a more complex distribution. This is the goal of the “filling factor” keyword used in Cloudy. The global action of this factor is to artificially increase the geometrical size of the nebula. There is virtually no difference on observables between a model with Q_0 , S and ff_C and a model with $K_2^2 \times Q_0$, $K_2 \times S$ and ff_C/K_2 , where Q_0 is the number of ionizing photons emitted by the central source, S is a parameter describing all the sizes of the nebula (R_1 and R_2 for example in Eq. 5), and K_2 being a coefficient greater than 1. All the line intensities (absolute and relative), the angular sizes, and the images are exactly the same in both models. The nebula would be at a distance D in the first case and $K_2 \times D$ in the second. Once the existence of such a clumping factor is accepted, then there is no way to determine the distance to the nebula, nor the absolute luminosity of the star, contrary to what is claimed by Monteiro et al. (2005) or Gesicki et al. (2006).

Using a filling factor of 1.0 as first guess, we determine the following parameters: The H β flux value (without reddening) is predicted to be $7.2 \times 10^{-10} \text{ erg cm}^{-2} \text{ s}^{-1}$. The distance is estimated to be $K_2 \times 1.26 \text{ kpc}$. The ionized hydrogen mass is $K_2^2 \times 0.057$ solar mass. With an equatorial radius of $K_2 \times 1.1 \times 10^{17} \text{ cm}$ and considering an expansion velocity of 30 km/s (see Sec. B), the age of the nebula is $K_2 \times 1400$ years. The stellar luminosity is $K_2^2 \times 7685$ solar luminosities and the corresponding number of ionizing photons is $K_2^2 \times 10^{47.6} \text{ s}^{-1}$.

Due to the presence of stellar wind, it is impossible to obtain the absolute luminosity of the star and so likewise impossible to determine a spectroscopic distance.

The distance to IC418 have been recently determined by Guzmán et al. (2009), using parallax expansion between two VLA observations with more than 20 years of delay. They determine a distance of $1.3 \pm 0.4 \text{ kpc}$. This value leads to a determination of the parameter K_2 close to unity and the other K_2 -dependant parameters as given in Tab. 1.

In the following section we present an independent (and more indirect) way to determine the distance to the PN.

5.4. Using evolutionary tracks to determine the distance

Once the effective temperature is known and using the evolutionary tracks from Vassiliadis & Wood (1994) or Bloeker (1995), a simple relation between the stellar luminosity and the evolutionary age of the nebula can be obtained. For T_{eff} close to

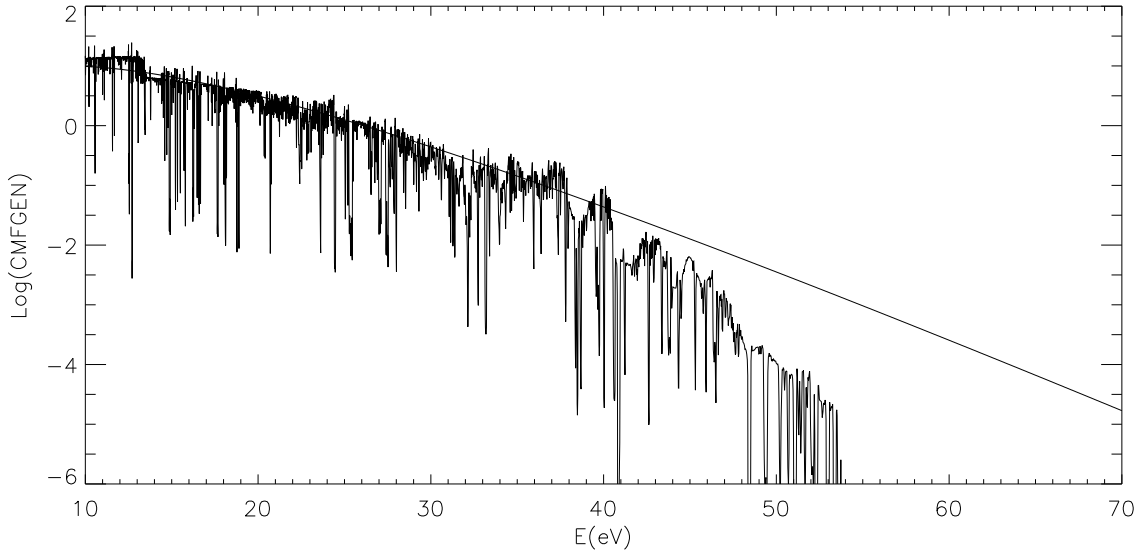


Fig. 10. This is the comparison between the CMFGEN model and a blackbody at 39.5 kK.

36.7 kK, the relation is $\log(\text{age}) = 17.34 - 3.73 \times \log(L/L_{\odot})$ from Vassiliadis & Wood (1994) and $\log(\text{age}) = 20.6 - 4.53 \times \log(L/L_{\odot})$ from Bloeker (1995).

On the other hand, from Sec.5.3 we determined the age as $K_2 \times 1400$ years and the luminosity as $K_2^2 \times 7685$ solar luminosities. Then we have: $\text{age}(\text{years}) = 1400 \times \sqrt{L/7685}$, similar to $\log(\text{age}) = 1.20 + 0.5 \times \log(L/L_{\odot})$.

The intersection of this relation with the ones determined from evolutionary tracks lead to a determination of the age, the luminosity, and all the parameters depending on K_2 . A value of $K_2 = 0.92$ (0.97) is found when using Vassiliadis & Wood (1994) (Bloeker 1995, resp.), leading to a clumping factor very close to 1.

The results presented in this section strongly depend on the evolutionary tracks on one hand, but on the other hand also on the determination of the dynamical age of the nebula. This latest is supposed to be the ratio of the size of the nebula with the expansion velocity. This implicitly assumes that the expansion velocity is constant over the expansion time of the nebula, which is the simplest hypothesis. Recent observations from Richer et al. (2008) seems to indicate that the expansion is accelerating, confirming theoretical results on the RAM pressure acceleration of the AGB envelope (García-Segura et al. 2006, and references therein). In this case, the age we determine from the line profiles is only an upper limit of the real dynamical age of the nebula, and this will induce a shift in the position of IC418 in the evolutionary tracks. For example, if we consider that the expansion velocity is only half the value we used in the previous section, to take into account the acceleration, the value obtained for K_2 is reduced by 0.03 dex. Notice that this decrease of the mean expansion velocity leads to a value of K_2 lower than 1., and the corresponding filling factor will be $1/K_2 > 1.0$.

The method presented in this section to determine a distance from the evolutionary tracks clearly depends on the reliability of these latest. The fact that the results are very comparable when using the tracks from Vassiliadis & Wood (1994) or from Bloeker (1995), that the derived filling factor is close to unity and that the distance is comparable to the one obtained by the parallax method by Guzmán et al. (2009) tends to indicate that

the evolutionary tracks are trustable, at least in the part of the HR-diagram where IC418 lives.

5.5. Comparing the stellar and the nebular abundances

The nebula is found to be Carbon- and Nitrogen-rich (0.5 and 0.2 dex over the solar value respectively) while the Oxygen abundance is close to solar (0.05 dex lower). The Neon and Argon abundances are close to the solar value. Magnesium, Silicon, Sulfur and Chlorine are deficient by 0.5 dex relative to their solar values, while Iron is deficient by 2.9 dex, suggesting the depletion of those elements in dust grains (whose presence is supported by the IR continuum emission). The nebular helium abundance is 0.2 dex greater than the solar value.

The star is also found to be Carbon-rich. The value obtained for C/O (by mass) are comparable: 1. and 1.5 for the star and the nebula respectively. The uncertainty in C/H is quite large in the case of the nebular value. If we only consider the recombination lines of C, we would obtain a higher value for C/H, while the forbidden lines lead to a lower value. A better agreement between the stellar and the nebular value for C/O is then obtained when using only the forbidden lines.

We actually made a test model adopting the same abundance for the star and the nebula (adopting a mean value between the two abundances), and the model was not able to fit the observations. This give us an indication that the differences between the star and the nebula are larger than the tolerance we could adopt in the fit of the observations.

We can also point out that the presence of the X-ray component (Sec.A) is not taken into account in the stellar model process. The real ionization state of the irradiated atmosphere can be higher than the one predicted by the model. The effect on the abundances determined for the star is hard to estimate, but would be in the sens of an underestimation of the real abundances.

The composition of the nebula should reflect the composition of the star in the epoch it was ejected. Therefore the observed differences in the compositions should reflect the evolution of the star after the ejection. First of all the He abundance in the star is elevated with respect to the nebula. One possible reason for this is the stellar wind. The star is loosing part of its

hydrogen envelop increasing the relative abundance of Helium. Carbon is enriched both in the star and the nebula which means that the nebula was ejected after the third dredge up (TDU) when the carbon rich material is exposed at the surface. The Nitrogen abundance is slightly increased but $N/O \sim 0.1$. This low value, together with the normal oxygen composition means that no hot bottom burning (HBB) had happened (Karakas et al. 2009). The small increase of N can be attributed to TDU and mixing from a incomplete H burning shell (Cristallo et al. 2009). Thus, CNO abundances are in accordance with the progenitor mass less than 4.0 (the limit for the HBB). In the previous section we calculated the age of the nebula and the luminosity of the star from the evolutionary tracks. The solution obtained there leads to progenitor mass of 1.75 M_{\odot} and 3.0 M_{\odot} calculated with the tracks of Vassiliadis & Wood (1994) and and Bloeker (1995) respectively. Thus, the progenitor mass is in agreement with the CNO abundances.

6. Conclusion

In this paper we present a combined, stellar and nebular model of the Planetary Nebula IC418 that reproduces all the observational material available: optical and UV stellar observations (lines and continuum) and IR, deep optical and UV emission line observations as well as HST images for the nebula. A total of 140 emission lines are considered, most of them being pure predictions of the model (i.e. are not used for the convergence process).

The use of a 3D photoionization model for the nebula is not crucial for the description of the morphology, as IC418 is close to spherical, but it is of first importance to take into account the effect of the position, size and orientation of the apertures used for the different observations. The apertures are used as masks over the emission line surface brightness maps to compute the line intensities. The apparent discrepancies between the intensities of a given line reported by different authors is sometime well reproduced when these slit effects are taken into account.

The agreement between the stellar atmosphere model performed using the CMFGEN code and the photoionization models obtained by Cloudy_3D is impressive: the high ionization potential ions (Ne^{2+} and Ar^{3+}), whose lines are overpredicted when using a simple Planck function as the SED, are perfectly reproduced when a stellar atmosphere model is used. This is as a result of the effect of line blanketing in the > 40 eV region that reduces drastically the ionic fraction of these ions.

The possible presence of clumps in the nebula leads to a degeneracy between the distance, the luminosity, and the clumping factor. It is a priori impossible to resolve this discrepancy in the case of IC418 because no spectroscopic distance can be obtained due to another degeneracy between the stellar luminosity and the mass loss rate. Nevertheless, using the distance determined by the parallax method by Guzmán et al. (2009), we can resolve the degeneracy and conclude that there are no clumps in the nebula.

We found that evolutionary tracks allows us to another more indirect determination of the distance, close to 1.25 kpc and an age of 1400 years. This distance is in very good agreement with the one obtain using parallax method.

High spectral nebular emission line profiles are reproduced by a velocity expansion law that strongly increases with the distance from the center of the nebula.

Reliable abundances are determined for the nebula and the star. We found the nebula to be Carbon- and Nitrogen-rich while the Oxygen abundance is close to solar, as are those of Neon and Argon. Magnesium, Silicon and Iron are highly deficient, suggesting the depletion of those elements in dust grains. Sulfur

and Chlorine are also deficient. The nebular Helium abundance is 0.2 dex higher than the solar value. The star is also found to be Carbon-rich.

Acknowledgements. We first of all wish to thank Vladimir Escalante who asked CM four years ago for a “quick” model of IC418... Here we are! We thank Juan Echevarria and Rafael Costero for providing optical stellar spectrum of IC418. We are very grateful to Grazyna Stasińska, Michael Richer, Svetozar Zhekov, Jorge Garcia Rojas and Luc Binette for useful discussions and a careful reading of the manuscript. We also wish to thank Elena Jimenez Bailon for her help on the analysis of the Chandra observations. The computations were carried out on a AMD-64bit computer financed by grant PAPIIT IX125304 from DGAPA (UNAM,Mexico). This work is partly supported by grants CONACyT-40095, CONACyT-48737, CONACyT-49749 and CONACyT-60967 (Mexico).

References

- Aller, L. H. & Czyzak, S. J. 1983, *ApJS*, 51, 211
 Aller, L. H., Keyes, C. D., Ross, J. E., & Czyzak, S. J. 1980, *Ap&SS*, 67, 349
 Asplund, M., Grevesse, N., & Sauval, A. J. 2005, in *Astronomical Society of the Pacific Conference Series*, Vol. 336, *Cosmic Abundances as Records of Stellar Evolution and Nucleosynthesis*, ed. T. G. Barnes, III & F. N. Bash, 25–+
 Beck, S. C., Lacy, J. H., Townes, C. H., et al. 1981, *ApJ*, 249, 592
 Bloeker, T. 1995, *A&A*, 299, 755
 Buerger, E. G. 1973, *ApJ*, 180, 817
 Cristallo, S., Straniero, O., Gallino, R., et al. 2009, *ApJ*, 696, 797
 Ercolano, B., Wesson, R., Zhang, Y., et al. 2004, *MNRAS*, 354, 558
 Escalante, V. & Morisset, C. 2005, *MNRAS*, 361, 813
 Ferland, G. J., Korista, K. T., Verner, D. A., et al. 1998, *PASP*, 110, 761
 Fitzpatrick, E. L. 1999, *PASP*, 111, 63
 García-Segura, G., López, J. A., Steffen, W., Meaburn, J., & Manchado, A. 2006, *ApJ*, 646, L61
 Gesicki, K., Acker, A., & Szczerba, R. 1996, *A&A*, 309, 907
 Gesicki, K., Zijlstra, A. A., Acker, A., et al. 2006, *A&A*, 451, 925
 Gutiérrez-Moreno, A., Cortes, G., & Moreno, H. 1985, *PASP*, 97, 397
 Guzmán, L., Loinard, L., Gómez, Y., & Morisset, C. 2009, *AJ*, 138, 46
 Handler, G., Mendez, R. H., Medupe, R., et al. 1997, *A&A*, 320, 125
 Henry, R. B. C., Kwitter, K. B., & Bates, J. A. 2000, *ApJ*, 531, 928
 Hillier, D. J., Lanz, T., Heap, S. R., et al. 2003, *ApJ*, 588, 1039
 Hillier, D. J. & Miller, D. L. 1998, *ApJ*, 496, 407
 Hyung, S., Aller, L. H., & Feibelman, W. A. 1994, *PASP*, 106, 745
 Karakas, A. I., van Raai, M. A., Lugaro, M., Sterling, N. C., & Dinerstein, H. L. 2009, *ApJ*, 690, 1130
 Keenan, F. P., Aller, L. H., Exter, K. M., Hyung, S., & Pollacco, D. L. 2003, *ApJ*, 584, 385
 Krueger, T. K. & Czyzak, S. J. 1970, *Royal Society of London Proceedings Series A*, 318, 531
 Kudritzki, R. P., Mendez, R. H., Puls, J., & McCarthy, J. K. 1997, in *IAU Symposium*, Vol. 180, *Planetary Nebulae*, ed. H. J. Habing & H. J. G. L. M. Lamers, 64–+
 Macfarlane, J. J., Cohen, D. H., & Wang, P. 1994, *ApJ*, 437, 351
 Marigo, P., Bernard-Salas, J., Pottasch, S. R., Tielens, A. G. G. M., & Wesselius, P. R. 2003, *A&A*, 409, 619
 Mendez, R. H., Forte, J. C., & Lopez, R. H. 1986, *Revista Mexicana de Astronomia y Astrofisica*, 13, 119
 Mendez, R. H., Kudritzki, R. P., Herrero, A., Husfeld, D., & Groth, H. G. 1988, *A&A*, 190, 113
 Monteiro, H., Schwarz, H. E., Gruenwald, R., Guenther, K., & Heathcote, S. R. 2005, *ApJ*, 620, 321
 Morisset, C. 2006, in *IAU Symposium*, Vol. 234, *Planetary Nebulae in our Galaxy and Beyond*, ed. M. J. Barlow & R. H. Mendez, 467–468
 Patriarchi, P. & Perinotto, M. 1995, *A&AS*, 110, 353
 Pauldrach, A. W. A., Hoffmann, T. L., & Méndez, R. H. 2004, *A&A*, 419, 1111
 Péquignot, D., Ferland, G., Netzer, H., et al. 2001, in *Astronomical Society of the Pacific Conference Series*, Vol. 247, *Spectroscopic Challenges of Photoionized Plasmas*, ed. G. Ferland & D. W. Savin, 533–+
 Pottasch, S. R., Bernard-Salas, J., Beintema, D. A., & Feibelman, W. A. 2004, *A&A*, 423, 593
 Prinja, R. K., Hodges, S. E., Massa, D. L., Fullerton, A. W., & Burnley, A. W. 2007, *MNRAS*, 382, 299
 Richer, M. G., López, J. A., Pereyra, M., et al. 2008, *ApJ*, 689, 203
 Schönberner, D., Jacob, R., Steffen, M., et al. 2005, *A&A*, 431, 963
 Schmutz, W., Hamann, W.-R., & Wessolowski, U. 1989, *A&A*, 210, 236
 Sharpee, B., Baldwin, J. A., & Williams, R. 2004, *ApJ*, 615, 323
 Sharpee, B., Williams, R., Baldwin, J. A., & van Hoof, P. A. M. 2003, *ApJS*, 149, 157

- Sterling, N. C., Dinerstein, H. L., & Kallman, T. R. 2007, *ApJS*, 169, 37
- Tayal, S. S. 2000, *Atomic Data and Nuclear Data Tables*, 76, 191
- Tayal, S. S. 2006, *ApJS*, 163, 207
- Vassiliadis, E. & Wood, P. R. 1994, *ApJS*, 92, 125
- Wilson, N. J. & Bell, K. L. 2002, *MNRAS*, 331, 389
- Wright, N. J., Barlow, M. J., Ercolano, B., & Rauch, T. 2007, *ArXiv e-prints*, 709

Online Material

Appendix A: Presence of an X-ray component

The UV spectra exhibit a strong stellar O VI 1031,1037Å line (Fig. D.2) that can not be reproduced by a ~ 40 kK stellar atmosphere model. This line is classically explained by the Auger ionization due to X-ray emission produced by wind instabilities. A weak X-ray emission is confirmed by Chandra observations². The Chandra data reduction has been performed using the Ciao V3.4 package CALDB (updated in May 2007) following standard procedures. Images in the 0.5-1.5 keV, 1.5-2.5 keV and 2.5-8 keV bands were generated using “dmcopy” and “csmooth” Ciao procedures. Counts are only significantly detected in the softer energy band image (0.5-1.5 keV) indicating that the source is intrinsically soft.

The limited count detection (less than 40 photons) does not allow a spectral analysis. The soft energy flux (i.e. 0.5-2 keV band) is estimated assuming an emitting model of a black-body with a temperature of ~ 0.03 keV and taking into account a neutral absorption of $N_H = 2 \times 10^{21} \text{ cm}^{-2}$. The unabsorbed measured flux of the source in the 0.5-2 keV band is $1 \times 10^{-14} \text{ erg/s/cm}^2$.

To take this X-ray emission into account, we add a black-body emission at 300 kK to the stellar flux. We don't have any constraints on the shape of the X-ray emission, so we used the Planck function as the simplest SED.

This soft X-ray component doesn't change the determination of the nebular parameters, such as the abundances. It does have a small influence on the high Ionization Potential (IPs) emission lines ([Ne III] and [Ar IV]), which are slightly underestimated by the model if the X-ray component is not taken into account. We adjust the luminosity of the soft X-ray component so that these high IPs emission lines are reproduced. The required bolometric luminosity is $3 L_\odot$ (using 1.25 kpc for the distance), which corresponds to a flux in the 0.5-2 keV band of $4 \times 10^{-17} \text{ erg/s/cm}^2$, much lower than the observed X-ray flux. A hotter X-ray source would have a smaller luminosity to conserve the soft X-ray flux and has no influence on these lines. On the contrary, a cooler X-ray source would require a higher luminosity, leading to intensities of these high IPs lines higher than the observed values.

Appendix B: Line profiles

Gesicki et al. (1996) published observations at high spectral resolution of IC418 for the H β , [O III] 5007Å, and [N II] 6584Å lines. Sharpee et al. (2004) also report high resolution observations for various ions. In both cases, the H I profiles are broad, with an half width at half maximum (HWHM) close to 18 km/s, the [O III] lines are narrower, with a HWHM close to 9 km/s, while the low density species, such as [N II], show a double peaked profile, with an inter-peak spacing of 20 km/s and each peak with a HWHM comparable to the one of the single [O III] line.

We compute the line profiles and compare them to the observations of Gesicki et al. (1996) using the same aperture size and position they used, namely a centered square aperture of 3 arcsec size. Despite the fact that the density law determined by these authors in no way reproduces the observed surface brightness, we can fit an expansion velocity law similar to the one they adopt. The resulting profiles reproduce the main properties of the observed ones (see Fig. B.1). The velocity law we adopt here is $V \propto R^4$ with a maximum of 30 km/s at the outer edge of the nebula. It is beyond the scope of this paper to make a complete dynamical model of IC418. We only check that the morphology we used is not trivially ruled out by the line profile observations. The values for the velocities of O⁺⁺ and N⁺ we found are compatible with the radiation-hydrodynamic models presented by Schönberner et al. (2005).

Appendix C: Chlorine collision strengths and electron temperature diagnostic

The collision strengths for Cl⁺⁺ used in Cloudy are taken from Wilson & Bell (2002). Notice that Cloudy takes into account the correction by a factor of 10 for the collision strength for $^1\text{D}_2\text{-}^1\text{S}_0$ as discussed in Keenan et al. (2003). We test the values from this reference against the previous values from Krueger & Czyzak (1970) and found that the latest are in better agreement with the observations. On one side the values for [Cl II] and [Cl III] are fitted when using values from Krueger & Czyzak, while it's impossible to fit both ions with the same Cl abundance when using collision strengths from Wilson & Bell. In this case, the [Cl II] lines are predicted too high, while the [Cl III] lines are fitted.

On the other hand, the electron temperature diagnostic [Cl II] 6162/9124Å is found to be predicted coherent with the [S II] and one of the two [O II] diagnostic when using Krueger & Czyzak. For these low ionization lines, the model overpredicts the ratios with $\kappa([\text{S II}], [\text{Cl II}]) \sim 1.5$. Using the values from

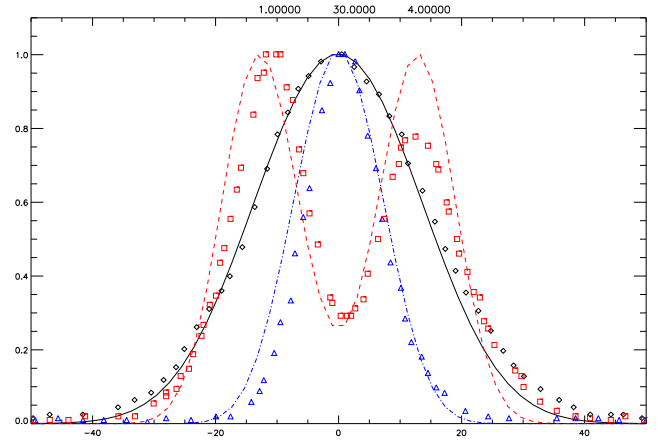


Fig. B.1. Emission line profiles: models (lines) and observations (Gesicki et al. 1996, symbols), for H β (black solid line and diamonds), [O III] 5007Å (blue dot-dashed line and triangles) and [N II] 6584Å (red dashed line and squares). Intensities are scaled so that the maximum of each profile reach 1.0.

Wilson & Bell leads to a prediction of the [Cl II] 6162/9124Å ratio lower than what is observed, with $\kappa([\text{Cl II}]) \sim -1.2$.

Appendix D: Online figures and tables

List of Objects

‘IC418’ on page 1

² ID: 7440, exposure time of 50 ks, obtained the 12th of December 2006

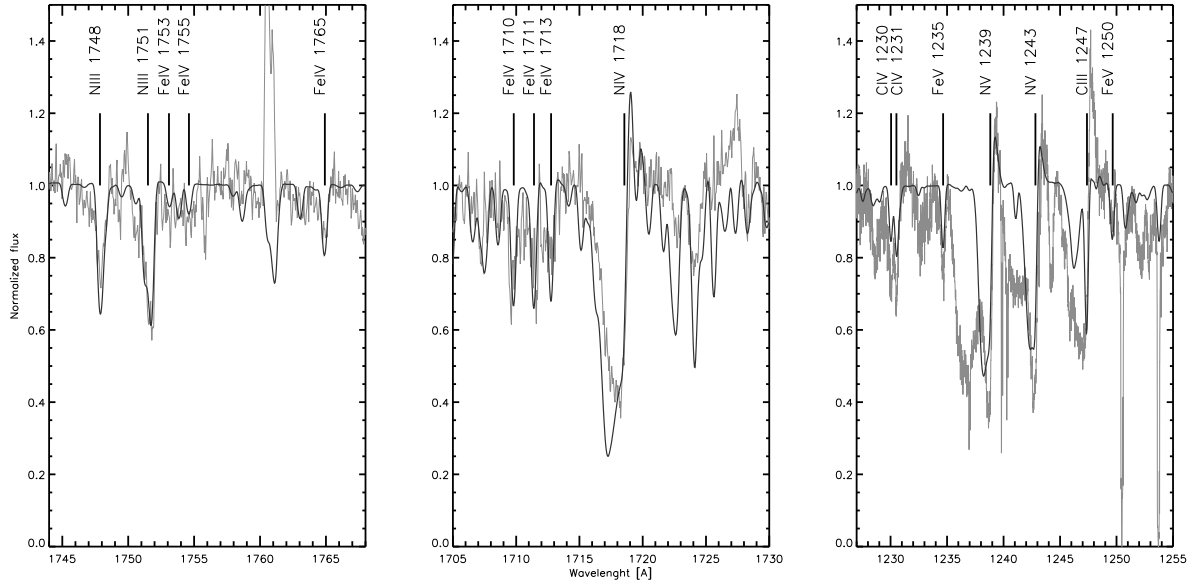


Fig. D.1. The fit to the Nitrogen and FeIV lines. Notice the nebular emission line C II 1761 Å.

Table D.1. Diagnostic ratios. I: Line ratio, II: Observed ratio, III : Ratio from the model , IV: Quality factor $\kappa(O)$ (See sec.4.3) for the model. All the density (temperature) diagnostic ratios are increasing with the electron density (temperature resp.). For the optical lines, HAF refers to Hyung et al. (1994), GCM to Gutiérrez-Moreno et al. (1985), and to Sharpee et al. (2003) otherwise.

I	II	III	IV
R O 2 2471/7325+	0.7635	0.7635	-0.00
Ne S 2 6731/6716	2.1250	2.0641	-0.12
Ne S 2 6731/6716 HAF	1.8914	2.0693	0.25
Ne S 2 6731/6716 GCM	2.0431	2.0588	0.02
Ne O 2 3726/3729	2.3653	2.5433	0.55
Ne O 2 3726/3729 HAF	2.4000	2.5500	0.24
Ne S 3 18.7/33.5	5.8102	6.1838	0.15
Ne Cl 3 5538/5518	1.9560	1.9852	0.04
Ne Cl 3 5538/5518 HAF	2.0000	2.0465	0.05
Ne Cl 3 5538/5518 GCM	2.2222	1.9420	-0.30
Ne O 3 51.9/88.4	6.3413	7.2426	0.33
Ne Ar 4 4740/4711	1.2000	1.7769	1.11
Te S 2 4068+/6731+	0.3915	0.5367	1.56
Te S 2 4068+/6731+HAF	0.3198	0.5540	1.92
Te Cl 2 6162/9124+	0.0108	0.0182	1.60
Te O 2 7320+/3727+	0.1433	0.1949	3.10
Te O 2 7320+/3727+HAF	0.2266	0.2042	-0.55
Te N 2 5755/6584+	0.0127	0.0124	-0.15
Te N 2 5755/6584+ HAF	0.0141	0.0128	-0.32
Te S 3 6312/9531+	0.0143	0.0133	-0.25
Te S 3 6312/9531+ HAF	0.0179	0.0141	-0.67
Te S 3 6312/18.7	0.0564	0.0543	-0.11
Te Ar 3 7136/8.99	1.1262	0.9620	-0.43
Te Ar 3 5192/7136+	0.0037	0.0036	-0.10
Te Ar 3 5192/7136+ HAF	0.0043	0.0037	-0.39
Te N 3 1750/57.4	0.1757	0.2336	0.58
Te O 3 4363/5007+	0.0033	0.0027	-0.68
Te O 3 4363/5007+ HAF	0.0045	0.0028	-1.32
Te O 3 4363/5007+ GCM	0.0045	0.0027	-1.40
Te O 3 5007+/88.3	119.1307	140.8424	0.49
Te O 3 5007+/88.3 HAF	47.9473	80.5872	1.45
Te Ne 3 3869+/15.5	0.4268	0.3934	-0.23
Te Ne 3 3869+/15.5 HAF	0.2828	0.1607	-1.47

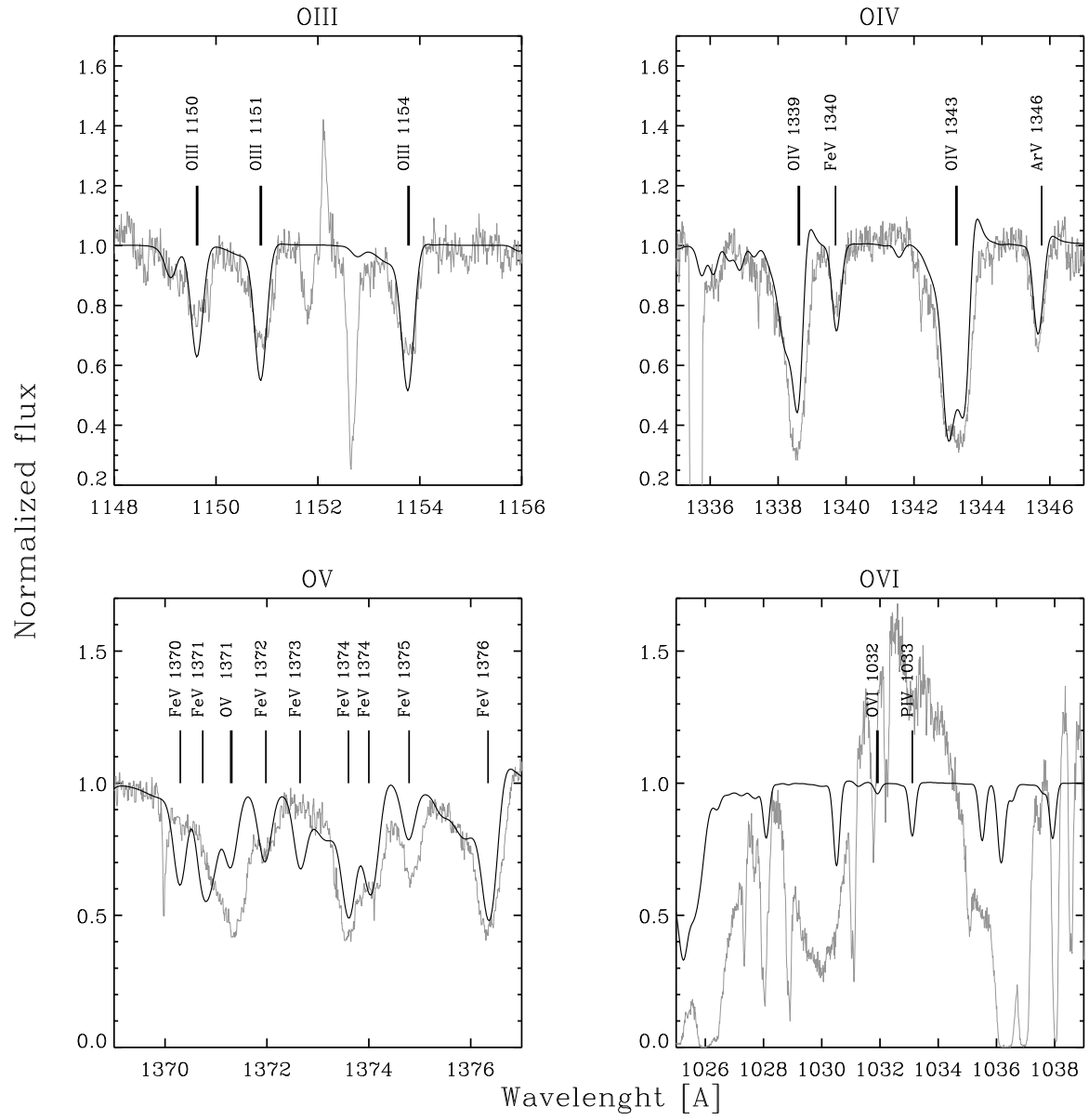


Fig. D.2. The fit to the Oxygen lines. Argon and some FeV lines are also indicated.

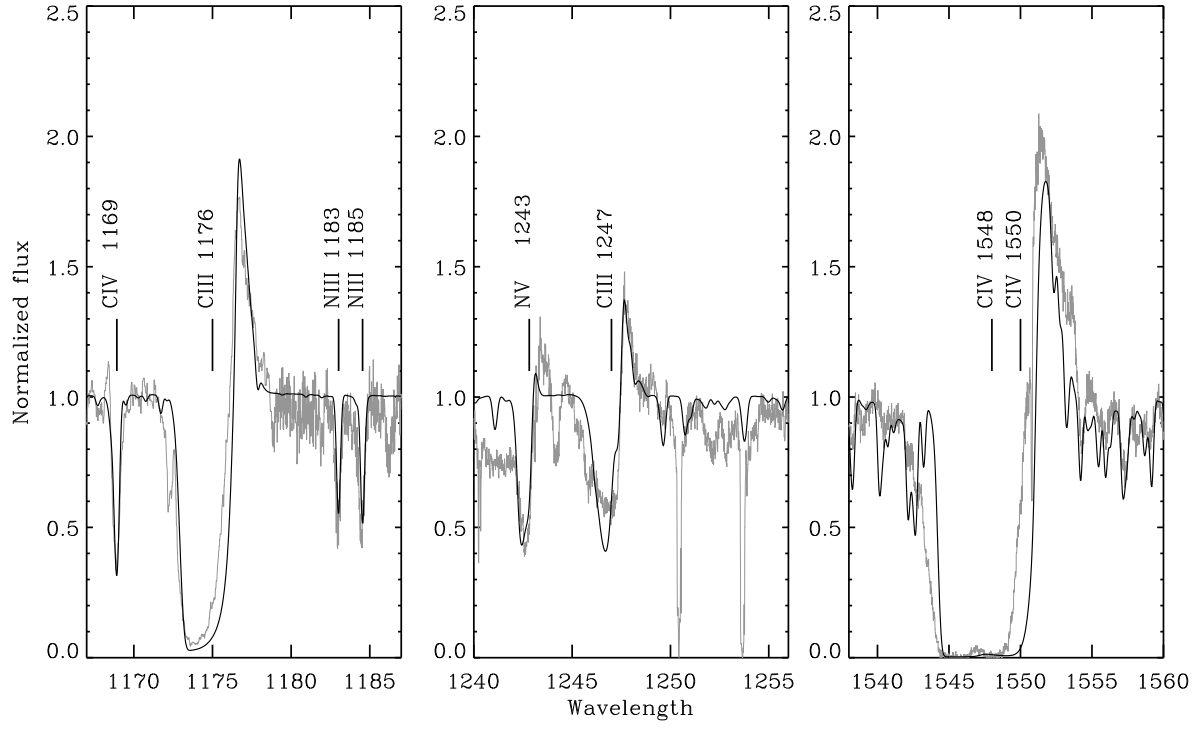


Fig. D.3. The fit to the Carbon lines. NIV 1183,85Å and NV 1188Å lines are also marked.

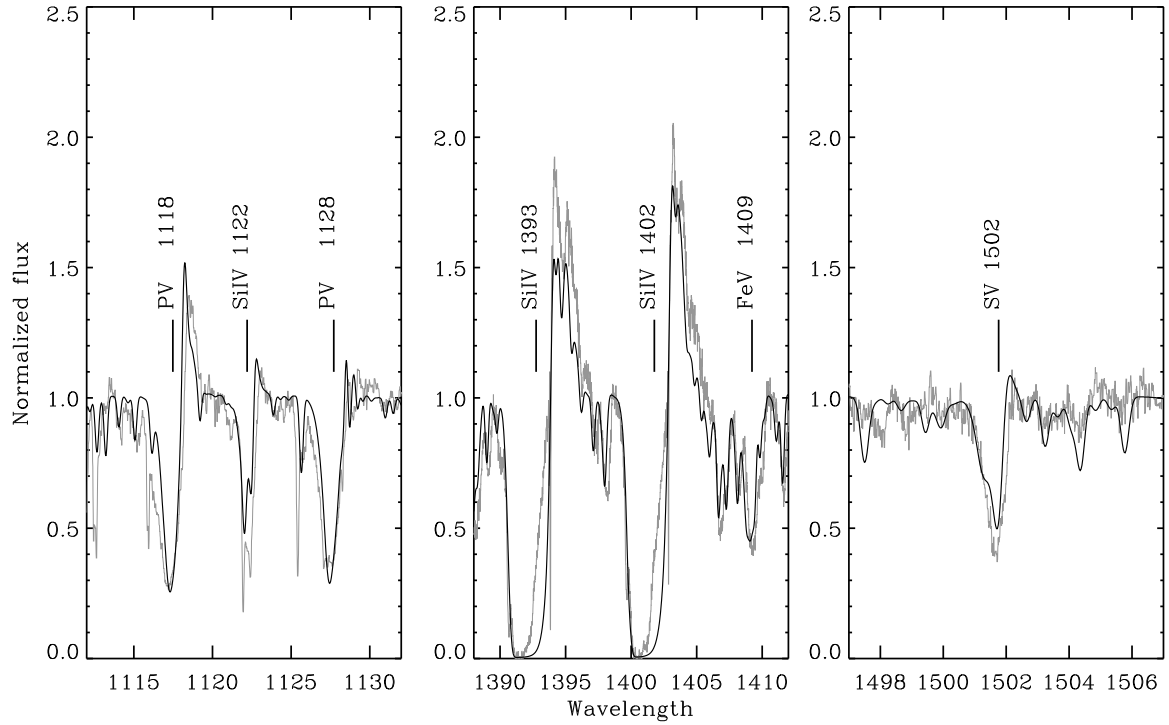


Fig. D.4. Phosphorus and silicon lines. Notice the strong absorption lines

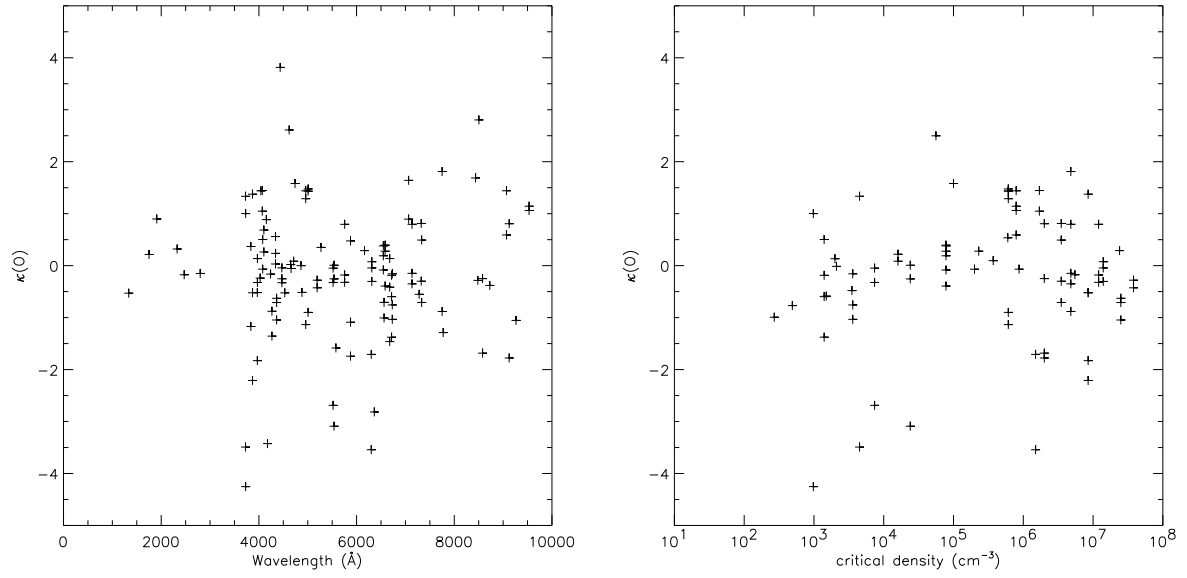


Fig. D.5. Quality factors $\kappa(O)$ vs. the wavelength (upper panel) and the critical density (bottom panel).

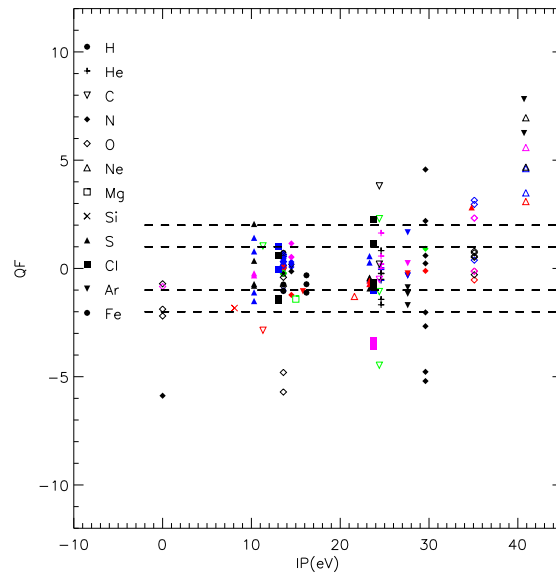


Fig. D.6. Same as Fig.6, but for blackbody Model.

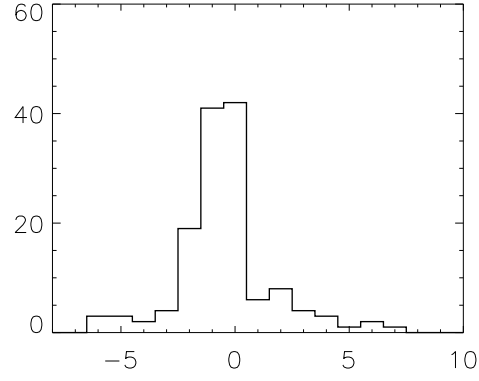


Fig. D.7. Same as Fig. 7, but for blackbody Model.

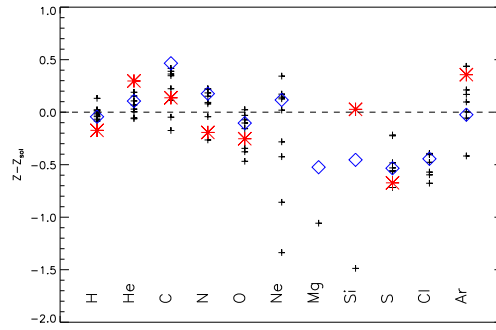


Fig. D.8. Nebular abundances by mass from the literature (small crosses, same as in Table 2) and from the adopted model (big stars for the stellar abundance and big diamond for the nebular abundances). Units are in number relative to the solar abundance from Asplund et al. (2005).